
Article:
Castelain, T, McCaig, AM and Cliff, RA (2014) Fluid evolution in an Oceanic Core Complex: a fluid inclusion study from IODP hole U1309 D - Atlantis Massif, 30°N, Mid-Atlantic Ridge. Geochemistry, Geophysics, Geosystems, 15 (4). 1193 - 1214. ISSN: 1525-2027

https://doi.org/10.1002/2013GC004975

AGU PUBLICATIONS

Geochemistry, Geophysics, Geosystems

RESEARCH ARTICLE

10.1002/2013GC004975

Key Points:
- The TAG model is a good analog for fluid evolution at Atlantis Massif
- Fluid inclusion analyses reveal evidence for magmatic exsolution
- Fluid inclusion analyses reveal evidence for phase separation

Correspondence to:
T. Castelain,
teddy.castelain@cnrs-orleans.fr

Citation:
Castelain, T., A. M. McCaig, and R. A. Cliff (2014), Fluid evolution in an Oceanic Core Complex: A fluid inclusion study from IODP Hole U1309 D—Atlantis Massif, 30°N, Mid-Atlantic Ridge, *Geochem. Geophys. Geosyst.*, *15*, 1193–1214, doi:10.1002/2013GC004975.

Received 2 AUG 2013
Accepted 14 JAN 2014
Accepted article online 20 JAN 2014
Published online 23 APR 2014

Fluid evolution in an Oceanic Core Complex: A fluid inclusion study from IODP hole U1309 D—Atlantis Massif, 30°N, Mid-Atlantic Ridge

Teddy Castelain[1], Andrew M. McCaig[2], and Robert A. Cliff[2]

[1]Institut des Sciences de la Terre d'Orléans, 1a rue de la Férollerie, Orléans, France, [2]School of Earth and Environment, Leeds University, Leeds, UK

Abstract In the detachment mode of slow seafloor spreading, convex-upward detachment faults take up a high proportion of the plate separation velocity exposing gabbro and serpentinized peridotite on the seafloor. Large, long-lived hydrothermal systems such as TAG are situated off axis and may be controlled by fluid flow up a detachment fault, with the source of magmatic heat being as deep as 7 kmbsf. The consequences of such deep circulation for the evolution of fluid temperature and salinity have not previously been investigated. Microthermometry on fluid inclusions trapped in diabase, gabbro, and trondjhemite, recovered at the Atlantis Massif Oceanic Core Complex (30°N, Mid-Atlantic Ridge), reveals evidence for magmatic exsolution, phase separation, and mixing between hydrothermal fluids and previously phase-separated fluids. Four types of fluid inclusions were identified, ranging in salinity from 1.4 to 35 wt % NaCl, although the most common inclusions have salinities close to seawater (3.4 wt % NaCl). Homogenization temperatures range from 160 to >400°C, with the highest temperatures in hypersaline inclusions trapped in trondjhemite and the lowest temperatures in low-salinity inclusions trapped in quartz veins. The fluid history of the Atlantis Massif is interpreted in the context of published thermochronometric data from the Massif, and a comparison with the inferred circulation pattern beneath the TAG hydrothermal field, to better constrain the pressure temperature conditions of trapping and when in the history of exhumation of the rocks sampled by IODP Hole U1309D fluids have been trapped.

1. Introduction

In previous studies, oceanic and ophiolitic fluid inclusions have been interpreted in the context of purely magmatic ocean floor spreading, with the principle driving force for hydrothermal circulation being a shallow axial magma chamber [*Kelley and Delaney*, 1987; *Kelley et al*., 1992, 1993]. The consequences for hydrothermal fluid circulation in Oceanic Core Complexes (OCCs) of the recently established "detachment mode" [*Escartin and Canales*, 2011; *McCaig and Harris*, 2012] of seafloor spreading have not been investigated. In particular, this mode of spreading may involve deeper magma chambers (up to 7 km below seafloor) [*deMartin et al*., 2007], focussed fluid discharge along detachment faults [*McCaig et al*., 2007, 2010], and exhumation of gabbros and peridotites onto the seafloor [*Cannat*, 1993; *Ildefonse et al*., 2007; *McCaig and Harris*, 2012].

Fluids of variable salinities have been found in ocean crust. Processes responsible for such variation have been widely investigated in previous studies. Two-phase separation has been suggested as an important process to explain the observed salinity variation of hydrothermal fluids (10–200% of the seawater value) at different localities in the Mid-Atlantic Ridge such as the MARK area (Mid-Atlantic Ridge at Kane) [*Kelley et al*., 1993], and in the South West Indian Ridge [*Kelley and Früh-Green*, 2001]. Nevertheless, other processes such as exsolution from a melt [*Kelley et al*., 1992; *Kelley and Malpas*, 1996] and hydration/dehydration reactions with precipitation/dissolution of associated chloride-bearing minerals [*Kelley and Robinson*, 1990] need to be considered in certain cases.

The Atlantis Massif (AM) is an Oceanic Core Complex (OCC) located at 30°N at the inside corner of the Mid-Atlantic Ridge (MAR) and the Atlantis Transform Fault (ATF). Gabbros and mantle peridotite were exhumed to the seafloor by the movement of a detachment fault that is the locus of hydrothermal fluid discharge [*Boshi et al*., 2006; *McCaig et al*., 2007, 2010]. IODP Hole U1309D has been drilled in the central dome of the AM which is believed to be the footwall of this major detachment fault. The drillcore shows evidence of fluid

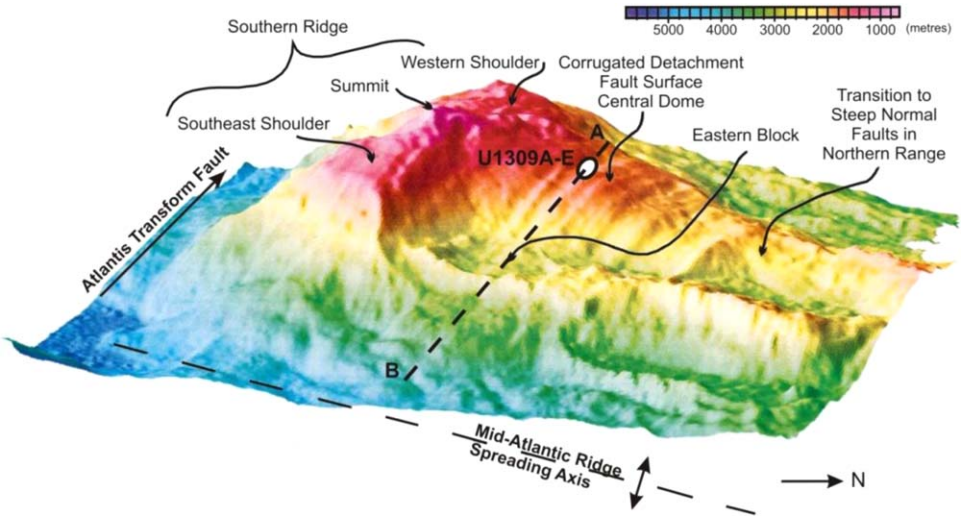

Figure 1. 3-D view of the Atlantis Massif showing morphotectonic features and the location of IODP holes U1309A-E. Illumination comes from SE. Vertical exaggeration is about 1.8. A color scale is shown to indicate the bathymetry [*Blackman et al*., 2006].

circulation, especially at depths <350 mbsf [*Blackman et al*., 2011]. Gabbros, diabases, and trondjhemite have trapped samples of hydrothermal fluids that might represent different fluids circulating in the AM during the exhumation and thermal evolution of the massif.

In this paper, we present analyses of fluid inclusions in gabbro, trondjhemite, and in quartz veins cutting diabase and trondjhemite recovered from IODP Hole U1309D from the central dome of the AM during the two consecutive IODP expeditions 304 and 305. Results are interpreted in a geodynamical context suggested by a model of the trans-Atlantic geotraverse (TAG) area [*deMartin et al*., 2007; *McCaig et al*., 2007, 2010]. They provide new insights on generation of brine and pressure-temperature constraints on the evolution of the hydrothermal fluid circulation in the Atlantis Massif and in OCCs [*Kelley*, 1996, 1997; *Vanko and Stakes*, 1991] in general.

2. Geological Setting

The Atlantis Massif is an OCC, located at the inside corner of the MAR and the ATF (30°N) (Figure 1). An OCC is a dome-like exposure of variably deformed and metamorphosed lower crustal and upper mantle rocks that has been unroofed by movement on a major detachment fault (Figure 2) [*Blackman et al*., 2002, 2011; *Ildefonse et al*., 2007; *Tucholke et al*., 1998; *McCaig and Harris*, 2012]. Gabbros from the massif have been dated between 1.08 ± 0.07 and 1.28 ± 0.05 Myr [*Grimes et al*., 2008].

The AM is composed of three different parts: (i) the central dome in which two deep holes (U1309B and U1309D) and five shallow-penetration holes (U1309A and U1309E-H), recovering upper sediment cover and fragments of detachment fault schist have been drilled (Figure 1), (ii) the southern wall which is dominated by serpentinized peridotite capped by a 100 m thick detachment shear zone rich in talc and tremolite [*Boschi et al*., 2006]; it is the host of the Lost City hydrothermal field, and (iii) the eastern block, interpreted as a fault-bounded block of basaltic material lying structurally above the central dome. The central dome is characterized by a corrugated surface believed to be an exposure of the major detachment fault responsible for the uplift of the massif. The corrugations are parallel to the spreading directions and have a wavelength of approximately 1000 m, amplitude of tens of meters, and length of several kilometers [*Cann et al*., 1997].

Hole U1309B (30°10.11′N, 42°07.11′W; 1642 mbsl) was drilled up to 101.8 mbsf with an average recovery of about 50%. Hole U1309D, located at 30°10.12′N, 40°07.11′W, 1645 mbsl, (20 m from Hole U1309B) penetrated 1415.5 mbsf, with a recovery of 75% comprising intrusive basalt and diabase (3%), gabbroic (91%), and olivine-rich rock (5%) consisting of dunites, wehrlites, troctolites, as well as a few mantle peridotites

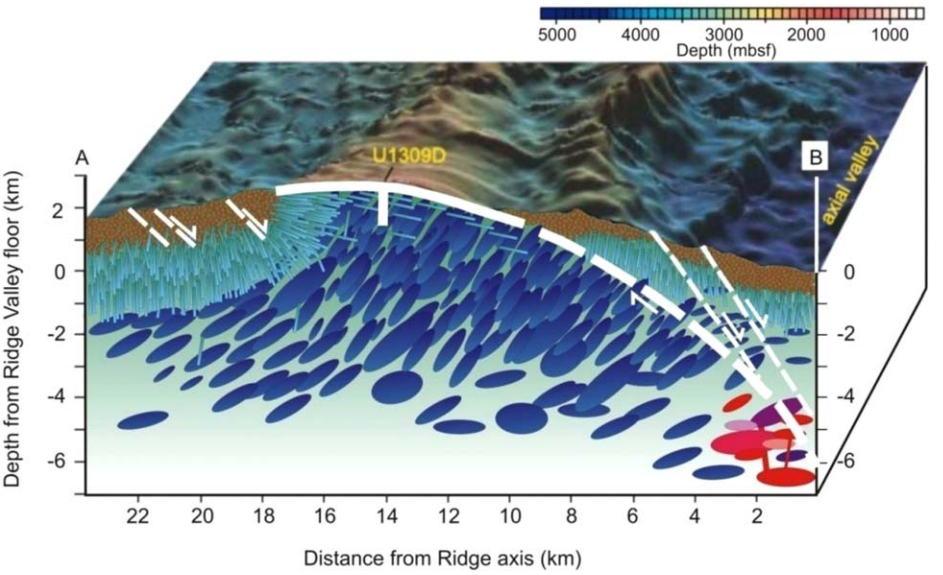

Figure 2. Schematic 3-D block diagram of the Atlantis Massif. Detachment fault is shown as a curved white line which steepens at depth. Location of U1309D is also shown in white. Red bodies represent active zones of intrusions. Blue sills are gabbro bodies intruding each other and forming the plutonic sequence of the lithospheric crust. Dikes also intrude one another and are shown in blue green. Pillow lavas lie on top of the dikes at the breakaway of the fault and in the hanging wall, but dikes also intrude into the footwall gabbros close to the fault (from *Grimes et al.* [2008]).

(harzburgite) in the upper 200 m. Seismic tomography suggests that a gabbro body several kilometers across forms the core of the massif, with relatively steep contacts against serpentinized peridotite to the south and west [*Canales et al*., 2008; *Henig et al*., 2012]. The drillcore recovered at Hole U1309D records strong evidence of penetration of altering fluids. Alteration occurred over a range of temperatures ranging from granulite facies to zeolite facies, but was dominantly in the greenschist and lower amphibolite facies [*Blackman et al*., 2011]. A few samples of detachment-related talc-tremolite schists were sampled in the uppermost 20 m of IODP Holes 1309B and 1309D, and fault breccias derived from diabase and gabbro are common in the upper 120 m of the holes [*Blackman et al*., 2006, 2011]; there is no doubt that the holes were drilled into the footwall of the detachment fault observed in outcrop at the summit of the south wall.

Gabbros in U1309B and U1309D vary in grain size (microgabbro to coarse grained gabbro) and deformation type, and can also be divided in several groups: microgabbro, oxide gabbro, gabbronorite, gabbro, olivine gabbro, troctolitic gabbro, and troctolite [*Blackman et al*., 2006]. Overall, the gabbros are equigranular, but can exhibit different types of deformation ranging from (rare) mylonitic to absolutely undeformed. Plagioclase is generally unaltered, but can show evidence of albitization in the vicinity of veins and magmatic intrusions and can also be altered to chlorite along fractures and in a corona reaction with olivine. Clinopyroxene rarely survives alteration in the upper 350 m of the Hole and is replaced by amphiboles (hornblende, actinolite, and tremolite). When olivine is present, it is more or less replaced by amphibole to form coronas in the upper part of the core, and to serpentine often accompanied by rodingitization of plagioclase [*Frost et al*., 2008] at greater depths.

Schoolmeesters et al. [2012] have used U-Pb zircon crystallization ages [*Grimes et al*., 2008, 2011], U-Th/He zircon thermochronometry, and multicomponent magnetic remanence data [*Morris et al*., 2009] to constrain the cooling rates of the AM. It has been shown that the upper 800 m of the central dome at the AM cooled from ≈780°C to ≈250°C at a rate of $2895_{(+1276/-1162)}$°C/Myr, whereas the lower 600 m cooled at a slower rate of ≈$500_{(+125/-102)}$°C/Myr, from ≈780°C to present day temperatures. Rocks from the uppermost part of the hole appear to have cooled more slowly from ≈250°C to 190°C at a rate of ≈300°C/Myr due to the hydrothermal circulation along the detachment fault. These results imply a thermal structure of the AM such that the depth of the root of the detachment fault is 7 km. The depth of the 190°C isotherm resides around ∼1.5 kmbsf while the temperature at Moho depth of 4.5–5 km [*Blackman and Collins*, 2010] is >500°C. According to the exhumation model of *Schoolmeesters et al*. [2012], the depth of the 250°C, and 580°C isotherms along the detachment fault, respectively, are ≈3.75 kmbsf and ≈6 kmbsf.

3. Methods

3.1. Petrographic Methods

3.1.1. Transmitted Light Microscope

An Olympus transmitted light microscope was used to detect, categorize, and map the fluid inclusion populations. Polished thin sections were used to determine the mineralogy of the samples, textural relationship between minerals and the occurrence of fluid inclusions. Samples with too few fluid inclusions were discarded and those with quartz veins (present only in the upper 250 m of the Hole) were favored. Areas of interest for further study were identified in double-polished wafers and sketched and photographed in plane polarized light. Microthermometric analyses were conducted on these same wafers, broken into chips, on quartz, and plagioclase in areas where fluid inclusion populations exceeded 10 inclusions >5 μm. On the basis of these criteria six samples were selected for detailed study.

3.1.2. Electron Microprobe Analyses

Electron microprobe analyses were conducted using a Cameca® SX-50 fitted with three wavelength-dispersive spectrometers for full quantitative analyses and with an Oxford MicroAnalysis Division Link 10/55S Energy Dispersive System for reconnaissance of phases and qualitative analyses. Polished thin sections were carbon coated (10–15 nm) before analyses. The microprobe is calibrated with a certified jadeite (Na), a pure synthetic MgO (Mg), a pure synthetic Al_2O_3 (Al), wollastonite (Si, Ca), halite (Cl), a certified orthoclase (K), a pure synthetic rutile (Ti), chromite (Cr), rhodonite (Mn), and hematite (Fe). This calibration is cross checked against silicate standards such as diopside (Si, Ca, Na), almandine (Si, Al, Fe), K-feldspar (Si, Al, K), and albite (Si, Al, Na) before every silicate analyses sessions.

Chlorite analyses were used to estimate temperatures of formation based on *Cathelineau and Nieva* [1985]. The calculation uses the relationship between the $Al_{[iv]}$ of chlorite and the temperature which is given by the following equation:

$$T = \frac{Al_{[iv]} + 8.26 \times 10^{-2}}{4.71 \times 10^{-3}}$$

3.2. Fluid Inclusions Microthermometry

3.2.1. Sampling

Samples where fluid inclusions population could be related to a fracturing event and crystallization of chlorite and exceeds 10 inclusions >5 μm were chosen. Six samples met these criteria: a quartz vein in diabase (U1309D 1R-1 41–44; depth = 20.9 mbsf); a troctolitic gabbro (U1309D 5R-3 107–110; depth = 40 mbsf); a gabbro (U1309D 10R-1 127–129; depth = 61.5 mbsf); a troctolite (U1309D 40R-1 6–12; depth = 214.8 mbsf); a troctolite (U1309D 40R-1 17–19; depth = 214.9 mbsf); and a trondjhemite (U1309D 40R-1 21–24; depth = 215 mbsf) cut by a quartz vein.

3.2.2. Analytical Method

Microthermometry measurements were carried out on 300 μm thick double-polished wafers using an Olympus® BX-50 transmitted light microscope with a Linkam® THMSG 600 heating-freezing stage covering a range in temperature from -196 to $+400$°C. The stage is controlled by a Linkam TMS 93 programmer via the LinkSys software version 2.15. Observation of fluid inclusions can be made by looking directly down the microscope or on the computer screen via a JVC TK-C1380 color video camera. Synthetic fluid inclusions of CO_2 and of pure H_2O in quartz were used to calibrate the microthermometric stage at temperatures of -56.6°C (triple point temperature of CO_2), 0.0°C (triple point of pure H_2O), and $+374.1$°C (critical point of pure H_2O). Calibration was always checked before each set of measurements. If variations in any of the three temperatures of calibration used were observed, necessary adjustments were made. Inclusions believed to have undergone processes such as necking down, stretching, and decrepitation that can change the volume of the cavity [*Roedder*, 1984], were not included in the statistics.

Repeated homogenization and freezing measurements were undertaken on individual inclusions in order to observe phase changes (such as ice melting point, halite dissolution temperature, liquid-vapor homogenization temperature) and to obtain homogenization temperatures and fluid salinities (in wt % NaCl eq). Salinities were calculated using the temperature of melting of ice for low-salinity fluids [*Bodnar*, 1993]. Salinities for saturated fluids were calculated using the temperature of dissolution of solid halite [*Sterner*

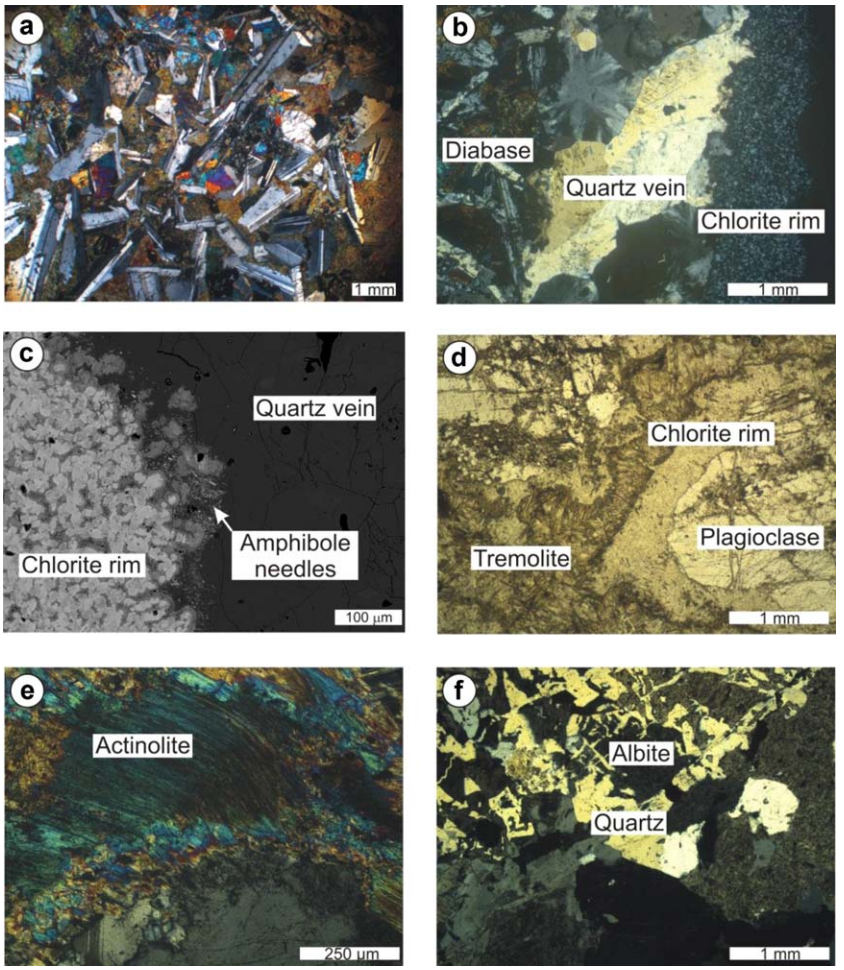

Figure 3. Photomicrographs; (a) ophitic texture of diabase with laths of plagioclase, green hornblende, and clinopyroxene relics as bright colors (sample U1309D 16R-2 58–61 piece 4, cross-polarized light). This sample is similar to the sample in which microthermometry was performed except that the grain size is coarser in that one. (b) Quartz-chlorite vein in diabase (sample U1309D 1R-1 41–44 piece 1, cross-polarized light). (c) Back scattered electron photomicrograph showing the vermiform chlorite of the quartz-chlorite vein and the amphibole needle intergrowth in sample U1309D 1R-1 41–44 piece 1. (d) Troctolitic gabbro showing corona texture—tremolite replaces olivine and chlorite replaces plagioclase (sample U1309D 5R-3 107–110, plane-polarized light (Figure 3c) and cross-polarized light (Figure 3d)). (e) Actinolite replacing clinopyroxene in troctolitic gabbro (sample U1309D 5R-3 107–110, piece 12, cross-polarized light). (f) Graphic texture of trondjhemite (sample U1309D 40R-1 21–24, piece 5, cross-polarized light).

et al., 1988]. Ice melting temperatures were reproducible to ±0.1°C, giving an error of ±0.17 wt % NaCl eq for unsaturated inclusions. Halite dissolution temperatures were reproducible to ±0.5°C giving an error of ±0.03 wt % NaCl equivalent. Homogenization temperatures were reproducible to ±1°C.

4. Results

4.1. Petrography of Samples From This Study

4.1.1. Quartz Vein in Diabase

Sample U1309D 1R-1 41–44 (depth = 20.9 mbsf) is a subophitic medium grained diabase composed of laths of unaltered and fractured plagioclase 0.1–2.5 mm in length, with poikilitic augite generally partially replaced by green hornblende (Figure 3*a*). The chemistry of several laths of plagioclase is presented in Table 1. Close to the quartz-chlorite vein, laths of plagioclase tend to have an albitic core and intermediate edges (labradorite), whereas away from the vein (laths 3, 4, and 5), the opposite is observed. The amphibole in the diabase is green magnesiohornblende (Table 1). Ilmenite partially replaces magnetite.

A 3 mm wide quartz-chlorite vein crosscuts the general fabric of the matrix. The quartz vein is equigranular and quartz grains are commonly of irregular shape. They exhibit a radial extinction (Figure 3b). Chlorite

Geochemistry, Geophysics, Geosystems

10.1002/2013GC004975

Table 1. Electron Microprobe Analyses of Plagioclases and Amphiboles in Diabase Sample U1309D 1R-1 41–44[a]

Oxide wt.%	Core of Lath 1	Edge of Lath 1	Core of Lath 2	Edge of Lath 2	Core of Lath 3	Edge of Lath 3	Core of Lath 4	Edge of Lath 4	Core of Lath 5	Edge of Lath 5	Am1	Am2	Am3	Am4	Am5	Am6	Am7	Am8	Am9	Am10
SiO_2	67.26	54.79	68.17	53.70	51.81	68.88	51.79	60.96	52.39	61.50	46.34	49.25	48.39	50.77	49.12	49.16	49.43	47.55	50.35	48.55
TiO_2	0.00	0.06	0.00	0.04	0.09	0.00	0.08	0.00	0.07	0.00	0.33	0.40	0.39	0.31	0.14	0.39	0.30	0.34	0.42	0.49
Al_2O_3	21.29	27.98	20.33	28.49	30.69	20.60	30.56	24.20	29.37	24.38	7.98	5.93	7.10	4.40	4.77	5.70	4.89	6.30	6.00	5.77
Cr_2O_3											0.00	0.30	0.32	0.00	0.00	0.04	0.40	0.41	0.16	0.11
Fe_2O_3	0.03	1.03	0.11	1.08	0.61	0.20	0.59	0.76	1.02	0.54	3.70	1.18	2.17	2.52	3.61	3.09	2.82	5.05	3.55	2.95
FeO											14.89	14.85	12.60	12.63	15.01	12.49	12.53	12.01	7.97	12.35
MnO	0.00	0.00	0.07	0.01	0.04	0.00	0.04	0.04	0.01	0.08	0.12	0.08	0.25	0.24	0.25	0.27	0.26	0.37	0.26	0.27
MgO	0.00	0.13	0.00	0.16	0.23	0.00	0.15	0.04	0.15	0.02	10.56	12.12	12.94	13.94	11.77	13.30	13.40	12.73	16.35	13.21
CaO	1.78	11.46	0.69	11.75	13.98	1.02	13.90	6.21	12.61	6.39	12.31	12.64	12.03	11.96	11.60	11.42	11.77	10.95	10.80	12.00
Na_2O	10.46	5.25	10.95	4.93	3.64	11.02	3.63	8.16	4.52	7.98	0.92	0.67	1.19	0.75	0.70	0.98	0.92	1.34	1.16	1.05
K_2O	0.01	0.06	0.04	0.04	0.04	0.05	0.01	0.13	0.05	0.12	0.09	0.06	0.06	0.06	0.05	0.06	0.06	0.05	0.04	0.07
H_2O											1.97	1.99	2.01	2.04	1.92	2.00	1.96	1.98	2.00	1.94
F											0.07	0.09	0.07	0.04	0.20	0.07	0.16	0.09	0.18	0.18
Cl											0.00	0.00	0.01	0.00	0.00	0.03	0.00	0.00	0.01	0.00
Total	100.82	100.74	100.36	100.19	101.13	101.76	100.75	100.48	100.17	101.01	99.27	99.55	99.53	99.66	99.15	98.99	98.90	99.18	99.26	98.93
Si	2.921	2.464	2.966	2.432	2.334	2.959	2.340	2.705	2.380	2.711	6.926	7.259	7.094	7.401	7.317	7.237	7.295	7.040	7.232	7.174
$Al_{(IV)}$	1.090	1.483	1.042	1.520	1.629	1.043	1.627	1.266	1.572	1.267	1.074	0.741	0.906	0.599	0.683	0.763	0.705	0.960	0.768	0.826
$Al_{(VI)}$											0.332	0.289	0.322	0.158	0.154	0.226	0.147	0.140	0.248	0.178
Ti	0.000	0.002	0.000	0.001	0.003	0.000	0.003	0.000	0.002	0.000	0.037	0.044	0.043	0.033	0.015	0.044	0.033	0.038	0.045	0.054
Cr											0.000	0.035	0.038	0.000	0.000	0.005	0.046	0.048	0.018	0.012
Fe^{3+}	0.001	0.035	0.004	0.037	0.021	0.006	0.020	0.025	0.035	0.018	0.416	0.131	0.239	0.277	0.404	0.342	0.314	0.563	0.384	0.328
Fe^{2+}											1.861	1.830	1.545	1.540	1.870	1.537	1.546	1.487	0.957	1.526
Mn	0.000	0.000	0.003	0.000	0.002	0.000	0.002	0.002	0.000	0.003	0.015	0.010	0.032	0.030	0.032	0.033	0.033	0.047	0.032	0.034
Mg	0.000	0.008	0.000	0.011	0.015	0.000	0.010	0.002	0.010	0.001	2.352	2.664	2.828	3.031	2.614	2.919	2.949	2.809	3.501	2.910
Ca	0.083	0.552	0.032	0.570	0.675	0.047	0.673	0.295	0.614	0.302	1.972	1.996	1.889	1.868	1.850	1.802	1.861	1.737	1.663	1.900
Na	0.880	0.458	0.924	0.433	0.318	0.918	0.318	0.702	0.398	0.682	0.267	0.191	0.339	0.212	0.202	0.280	0.262	0.384	0.322	0.301
K	0.000	0.003	0.002	0.002	0.002	0.003	0.001	0.007	0.003	0.007	0.016	0.012	0.011	0.010	0.010	0.011	0.012	0.010	0.008	0.014
OH											1.968	1.959	1.967	1.980	1.908	1.962	1.927	1.959	1.915	1.917
F											0.031	0.041	0.031	0.020	0.092	0.031	0.073	0.041	0.082	0.083
Cl											0.001	0.000	0.002	0.000	0.000	0.008	0.000	0.000	0.003	0.000
Total	4.975	5.006	4.973	5.006	4.998	4.976	4.993	5.004	5.014	4.991	17.268	17.201	17.286	17.160	17.153	17.197	17.203	17.263	17.178	17.257
An%	8	56	3	58	69	5	68	30	62	30										
Name	Ab	Lb	Ab	Lb	Lb	Ab	Lb	And	Lb	And	MgHb	MgHb	MgHb	MgHb	MgHb	MgHb	MgHb	MgHb	MgHb	MgHb

[a]An% = anorthite percentage, and name indicates type of amphibole. Am = amphibole; Ab = albite; Lb = labradorite; And = andesine; MgHb = Magnesiohornblende.

forms vermiform and radiating aggregates (Figure 3c), primarily on one side of the vein, and shows three distinct growth phases; an early growth phase with Mg numbers in the range 32–40 (Table 2, Chl 1–4) at a temperature of 283 ± 5°C [*Cathelineau and Nieva*, 1985], a second phase with Mg numbers from 54 to 60 (Table 2, Chl 5–8) at a temperature of 259 ± 5°C [*Cathelineau and Nieva*, 1985], and a final phase with Mg numbers from 62 to 71 (Table 2, Chl 9–12) at a temperature of 242 ± 17°C [*Cathelineau and Nieva*, 1985]. Chlorite appears to largely predate quartz, which is often intergrown with amphibole needles (magnesio-hornblende) at the edge of the vein (Table 2, Am 1–3; Figure 3c). Fluid inclusions occur as irregular shaped primary (?) inclusions clustering in the clear central part of the quartz grains of the vein. They are two phase, liquid-dominated inclusions ranging in size from 5 to 10 μm.

4.1.2. Gabbro

Sample U1309D 5R-3 107–110 (depth = 39.9 mbsf) is a medium grained troctolitic gabbro exhibiting plagioclase grains of intermediate composition (Table 3); it contains corona textures in which olivine is replaced by tremolite and plagioclase is partially replaced by chlorite and cut by chlorite veins (Figure 3d*)*. Actinolite and magnesiohornblende replace clinopyroxene (Figure 3*e and* Table 3). Plagioclase is slightly deformed and exhibits subgrain boundaries and deformation twins. Sample U1309D 10R-1 127–129 (depth = 61.5 mbsf) is a mylonitized coarse gabbro composed of roughly 60% deformed, partially recrystallized plagioclase and 40% green-brown hornblende and actinolite, replacing clinopyroxene; the plagioclase is partially altered to chlorite. Granoblastic recrystallization affects the boundaries of amphibole grains suggesting that the shear zone was active at amphibolite facies conditions. In these two last samples, fluid inclusions occur as both regular and irregular shaped secondary inclusions in plagioclase that occur in trails decorating fractures and as larger cigar-shaped inclusions perpendicular to chlorite veins. They are two phase and liquid dominated, ranging in size from 10 to 20 μm.

Samples U1309D 40R-1 6–12 (depth = 214.9 mbsf) and U1309D 40R-1 17–19 (depth = 215.0 mbsf) are troctolites showing the same textural characteristics as samples U1309D 5R-3 107–110 with more abundant olivine and crosscutting quartz veins. Fluid inclusions in these samples occur as irregular shaped primary inclusions. They generally cluster in the central part of the quartz grains of the vein. These fluid inclusions are two-phase liquid-dominated ranging in size from 5 to 20 μm.

4.1.3. Trondjhemite and Crosscutting Quartz Vein

Sample U1309D 40R-1 21–24 is a fine to medium grained trondjhemite composed of albitic plagioclase and quartz. Both are usually anhedral and form graphic intergrowths (Figure 3f). Alteration minerals (traces of tremolite and titanite along the edges of the graphic intergrowths) are not common. A large number of apparently primary fluid inclusions have been studied in a single 5 mm quartz grain of the trondjhemite. Two populations are observed; one with irregular shaped liquid-dominated inclusions and the other one with halite daughter crystals. Halite-bearing inclusions are generally bigger than those without halite and are irregular in shape (20–50 μm).

A late crack-seal quartz vein 4–5 mm in width crosscuts this late leucocratic magmatic intrusion. Quartz grains are elongated and also show radial extinction. Fluid inclusions in the vein are generally distributed as clusters in the clear central part of the grains, and are interpreted as being primary in origin. They are of irregular shape ranging in size from 10 to 20 μm, with some reaching several 10s of μm. They do not contain halite crystals.

4.2. Fluid Inclusions Typology and Results

Four types of fluid inclusions have been identified in the samples studied (Figure 4). Table 4 summarizes the results obtained for homogenization temperature and salinity for each type of inclusion and material. Types of fluid inclusion are classified with the numbering used in *Kelley et al*. [1992]:

- Type 1 inclusions are liquid dominated with low salinity
  - Type 1a inclusions have seawater-like salinities
  - Type 1b inclusions have salinities depleted with respect to seawater
- Type 2 inclusions are vapor dominated with low salinity (but were not observed in this study)
- Type 3 inclusions have high salinity

Geochemistry, Geophysics, Geosystems

10.1002/2013GC004975

Table 2. Electron Microprobe Analyses of Chlorite and Amphiboles in the Quartz-Chlorite Vein of Sample U1309D 1R-1 41–44[a]

Oxide wt %	Chl1	Chl2	Chl3	Chl4	Chl5	Chl6	Chl7	Chl8	Chl9	Chl10	Chl11	Chl12	Am1	Am2	Am3
SiO_2	25.15	25.12	24.82	25.19	27.13	27.23	27.51	27.43	27.73	28.89	28.57	29.43	49.89	48.74	50.20
TiO_2	0.04	0.02	0.00	0.03	0.00	0.00	0.00	0.01	0.02	0.02	0.00	0.01	0.23	0.24	0.33
Al_2O_3	19.35	19.96	19.78	19.58	18.99	18.97	18.91	19.37	18.51	18.07	18.16	17.10	5.43	5.74	4.97
Cr_2O_3	0.00	0.00	0.01	0.01	0.00	0.00	0.03	0.02	0.00	0.01	0.02	0.00	0.02	0.02	0.08
Fe_2O_3													0.00	0.00	0.00
FeO	33.68	32.85	31.84	31.09	23.75	22.60	20.90	20.25	21.18	17.88	17.08	15.59	17.48	18.65	15.12
MnO	0.69	0.35	0.34	0.25	0.99	1.27	1.19	1.51	0.92	0.97	0.73	0.73	0.13	0.10	0.33
MgO	9.09	9.91	10.76	11.49	16.32	17.05	17.57	18.66	20.30	20.34	21.54	22.42	11.66	11.16	13.67
CaO	0.02	0.01	0.02	0.02	0.02	0.02	0.11	0.01	0.04	0.04	0.02	0.05	12.32	12.32	11.61
Na_2O	0.11	0.06	0.09	0.11	0.03	0.16	0.06	0.02	0.16	0.03	0.11	0.12	0.62	0.64	0.85
K_2O	0.04	0.02	0.06	0.05	0.02	0.07	0.02	0.03	0.10	0.04	0.07	0.10	0.08	0.06	0.03
H_2O	10.88	10.98	10.94	11.01	11.39	11.45	11.42	11.58	11.76	11.65	11.69	11.68	2.01	2.00	1.99
F													0.02	0.00	0.06
Cl													0.04	0.02	0.06
Total	99.05	99.28	98.66	98.83	98.63	98.82	97.73	98.87	100.72	97.93	97.98	97.22	99.92	99.68	99.29
Si	5.544	5.488	5.441	5.487	5.714	5.705	5.776	5.680	5.658	5.950	5.863	6.041	7.369	7.271	7.384
$Al_{(tot)}$	5.026	5.138	5.111	5.026	4.714	4.686	4.679	4.727	4.451	4.385	4.392	4.136			
$Al_{(iv)}$													0.631	0.729	0.616
$Al_{(vi)}$													0.314	0.280	0.246
Ti	0.007	0.003	0.000	0.005	0.000	0.000	0.000	0.002	0.002	0.003	0.000	0.001	0.026	0.027	0.037
Cr	0.000	0.001	0.002	0.001	0.000	0.000	0.005	0.003	0.000	0.001	0.003	0.000	0.002	0.003	0.009
Fe^{3+}													0.000	0.000	0.000
Fe^{2+}	6.208	6.001	5.837	5.662	4.184	3.961	3.669	3.507	3.614	3.080	2.930	2.676	2.160	2.327	1.860
Mn	0.129	0.065	0.064	0.047	0.176	0.225	0.212	0.264	0.160	0.169	0.127	0.127	0.016	0.012	0.041
Mg	2.989	3.228	3.517	3.732	5.127	5.328	5.500	5.761	6.175	6.246	6.590	6.860	2.568	2.482	2.998
Ca	0.005	0.003	0.004	0.004	0.005	0.006	0.025	0.003	0.008	0.009	0.005	0.011	1.949	1.969	1.829
Na	0.046	0.024	0.037	0.046	0.013	0.063	0.025	0.006	0.063	0.014	0.042	0.049	0.178	0.185	0.242
K	0.010	0.006	0.017	0.015	0.005	0.018	0.006	0.007	0.026	0.009	0.018	0.027	0.015	0.011	0.005
OH	16.000	16.000	16.000	16.000	16.000	16.000	16.000	16.000	16.000	16.000	16.000	16.000	1.980	1.994	1.956
F													0.011	0.000	0.029
Cl													0.010	0.006	0.014
Total	35.964	35.955	36.030	36.025	35.938	35.992	35.897	35.960	36.158	35.866	35.970	35.928	17.228	17.294	17.268
Mg#	32.0	34.7	37.3	39.5	54.0	56.0	58.6	60.4	62.1	65.8	68.3	71.0			
T(°C)	277.3	283.7	288.5	283.3	259.9	260.1	252.6	263.4	264.9	234.6	243.6	224.4			
Name													MgHb	MgHb	MgHb

[a]Name indicates type of amphibole. Chl = chlorite; Am = amphibole; MgHb = magnesiohornblende.

10.1002/2013GC004975

Table 3. Electron Microprobe Analyses of Plagioclases and Amphiboles in Gabbro Sample U1309D 5R-3 107–110[a]

Oxide wt %	Plg1	Plg2	Plg3	Plg4	Plg5	Plg6	Plg7	Plg8	Plg9	Plg10	Am1	Am2	Am3	Am4	Am5	Am6	Am7	Am8	Am9
SiO_2	48.39	48.10	49.92	48.34	47.93	47.89	48.17	48.79	48.65	48.12	56.19	47.23	58.51	46.61	41.40	57.10	57.66	57.36	48.55
TiO_2	0.00	0.00	0.00	0.04	0.01	0.00	0.07	0.00	0.02	0.00	0.01	0.54	0.00	0.47	0.03	0.00	0.02	0.00	0.78
Al_2O_3	33.51	32.96	32.14	33.16	33.39	33.17	33.19	33.04	32.40	33.40	0.81	10.30	0.09	10.94	15.44	0.58	0.55	0.36	9.45
Cr_2O_3											0.02	0.18	0.00	0.09	0.00	0.04	0.01	0.00	0.78
Fe_2O_3	0.17	0.29	0.13	0.47	0.45	0.20	0.34	0.26	0.35	0.33	0.70	2.94	0.00	4.14	4.70	0.00	0.50	0.13	1.42
FeO											4.19	3.54	3.28	2.99	10.60	6.74	4.77	3.63	6.23
MnO	0.00	0.03	0.00	0.00	0.03	0.00	0.00	0.03	0.00	0.06	0.19	0.09	0.14	0.09	0.21	0.25	0.28	0.24	0.13
MgO	0.06	0.05	0.03	0.03	0.08	0.03	0.05	0.04	0.04	0.03	21.27	18.24	22.61	18.03	11.04	21.31	21.52	22.08	17.80
CaO	16.66	16.66	15.52	17.11	16.59	16.93	16.56	16.53	15.50	16.84	12.58	12.22	13.24	12.08	12.16	12.58	13.04	13.29	10.64
Na_2O	2.27	2.29	2.90	2.02	2.12	2.12	2.11	2.15	2.54	2.00	0.21	2.20	0.09	2.22	2.39	0.17	0.14	0.13	1.78
K_2O	0.04	0.05	0.01	0.00	0.00	0.02	0.02	0.00	0.23	0.02	0.01	0.13	0.01	0.11	0.14	0.01	0.00	0.01	0.13
H_2O											2.12	2.12	2.19	2.12	2.01	2.17	2.18	2.16	2.10
Cl											0.04	0.01	0.02	0.01	0.10	0.01	0.00	0.00	0.09
Total	101.1	100.43	100.65	101.17	100.6	100.36	100.51	100.84	99.73	100.8	98.34	99.75	100.17	99.90	100.23	100.97	100.67	99.39	99.86
Si	2.195	2.199	2.265	2.194	2.186	2.190	2.197	2.215	2.233	2.190	7.894	6.674	8.000	6.590	6.089	7.885	7.927	7.946	6.869
$Al_{(IV)}$	1.791	1.776	1.719	1.774	1.795	1.788	1.784	1.768	1.753	1.792	0.106	1.318	0.000	1.410	1.911	0.094	0.073	0.054	1.131
$Al_{(VI)}$											0.029	0.400	0.014	0.413	0.765	0.000	0.016	0.005	0.445
Ti	0.000	0.000	0.000	0.001	0.000	0.000	0.002	0.000	0.001	0.000	0.001	0.058	0.000	0.050	0.004	0.000	0.002	0.000	0.083
Cr											0.003	0.020	0.000	0.010	0.000	0.004	0.001	0.000	0.087
Fe^{3+}	0.006	0.010	0.004	0.016	0.015	0.007	0.012	0.009	0.012	0.011	0.074	0.313	0.000	0.440	0.520	0.000	0.052	0.014	0.151
Fe^{2+}											0.493	0.419	0.375	0.353	1.304	0.778	0.549	0.420	0.737
Mn	0.000	0.001	0.000	0.000	0.001	0.000	0.000	0.001	0.000	0.002	0.023	0.011	0.016	0.011	0.026	0.029	0.032	0.028	0.015
Mg	0.004	0.003	0.002	0.002	0.005	0.002	0.003	0.003	0.003	0.002	4.455	3.847	4.615	3.801	2.421	4.388	4.411	4.560	3.754
Ca	0.810	0.816	0.755	0.832	0.811	0.830	0.810	0.804	0.762	0.821	1.893	1.853	1.941	1.830	1.916	1.862	1.920	1.972	1.613
Na	0.200	0.203	0.255	0.177	0.188	0.188	0.187	0.189	0.226	0.177	0.057	0.603	0.025	0.609	0.682	0.045	0.037	0.035	0.488
K	0.002	0.003	0.000	0.000	0.000	0.001	0.001	0.000	0.014	0.001	0.002	0.024	0.002	0.020	0.026	0.002	0.000	0.001	0.023
OH											1.990	1.999	1.996	1.999	1.975	1.999	2.000	1.999	1.979
Cl											0.010	0.001	0.004	0.001	0.025	0.001	0.000	0.001	0.021
Total	5.008	5.011	5.001	4.998	5.002	5.006	4.996	4.991	5.003	4.997	17.029	17.548	16.997	17.538	17.664	17.088	17.019	17.036	17.397
An%	81.4	82.0	75.6	83.5	81.7	83.2	81.3	80.8	76.5	82.6									
Name	Byt	Byt	Byt	Byt	Byt	Byt	Byt	Byt	Byt	Byt	Trem	Ed	Trem	Ed	Parg	Act	Act	Trem	MgHb

[a]An% = anorthite percentage, and name indicates type of amphibole. Plg = plagioclase; Byt = bytownite; Am = amphibole; Trem = tremolite; Ed = edenite; Parg = pargasite; Act = actinolite; MgHb = magnesiohornblende.

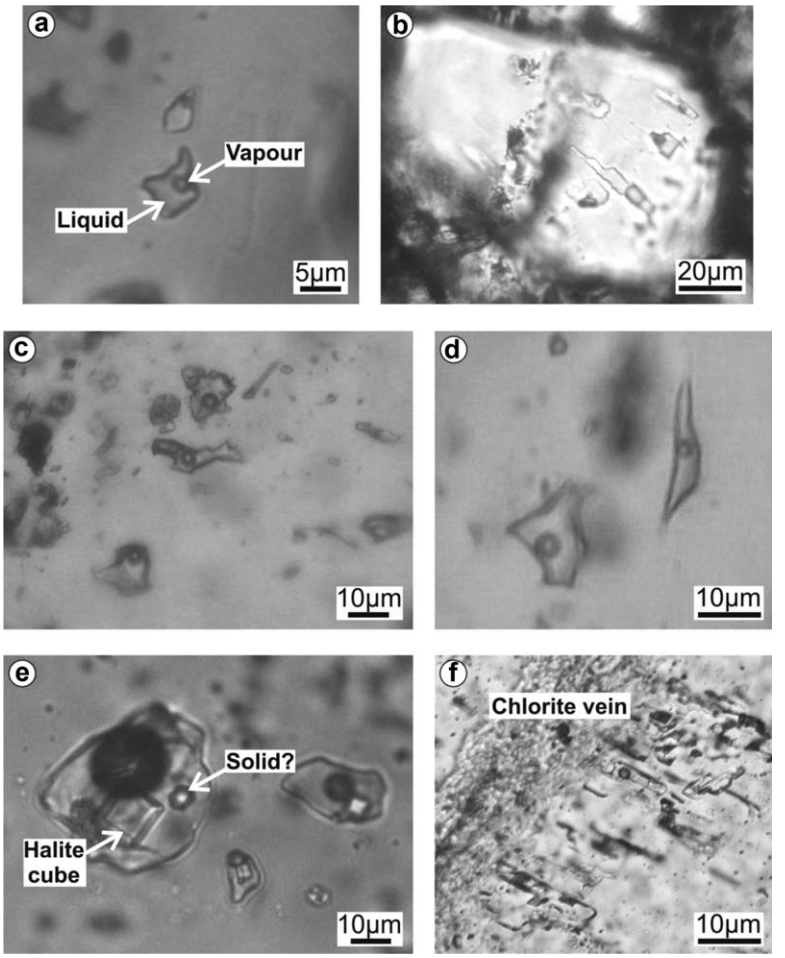

Figure 4. Photomicrographs of fluid inclusions. (a) Irregular shaped primary (?) fluid inclusions of type 1a (see section 4.2.1) in the quartz-chlorite vein of sample U1309D 1R-1 41–44. (b) Irregular shaped secondary fluid inclusions of type 1b (see section 4.2.1) in plagioclase of sample U1309D 10R-1 127–129. (c) Irregular shaped primary fluid inclusions of type 1a in quartz vein of sample U1309D 40R-1 17–19. (d) Irregular shaped primary inclusions of type 1a in quartz vein of sample U1309D 40R-1 21–24. (e) Halite-bearing fluid inclusions of type 3b (see section 4.2.3) in a quartz grain of a trondjhemite (U1309D 40R-1 21–24). Note that inclusions of fluid type 3a (see section 4.2.2) are similar in shape to inclusions of type 3b but do not host a halite cube. (f) Secondary cigar-shaped fluid inclusions in plagioclase related to chlorite vein in sample U1309D 5R-3 107–110.

- Type 3a inclusions are two-phase liquid-dominated inclusions
- Type 3b inclusions have halite daughter crystals

The primary/secondary origin of fluid inclusions was not always clear; nonetheless, fluid inclusions in quartz veins were usually concentrated in clusters in the center of the quartz grains and therefore interpreted as primary inclusions. In plagioclase and in quartz grains of the trondjhemite, fluid inclusions are secondary in origin as they are commonly decorating sealed fractures.

4.2.1. Type 1: Liquid-Dominated Low-Salinity Inclusions [L + V (L)]

Liquid-dominated, low-salinity inclusions have been found in all the samples in both quartz and plagioclase, and they generally occur as irregular inclusions ranging in size from 5 to 30 μm with the exception of sample U1309D 40R-1 17–19, where inclusions up to 100 μm in size have been found. Rare regular shaped inclusions are found in plagioclase grains. Irregular shaped inclusions might be the result of necking down, stretching, and/or leaking. Therefore, particular care has been taken to verify the similarity in behavior of irregular shaped inclusions relative to regular shaped ones. Where fluid inclusions exhibited salinities and/or homogenization temperatures significantly different from the other inclusions in the same population, those were not included in the statistics (11 out of 329). Results from sample U1309D 40R-1 6–12 are not included in the statistics either as only six measurements were undertaken in this sample.

Table 4. Fluid Inclusion Microthermometric Analyses[a]

Sample (U1309D)	Rock	Depth (mbsf)	Mineral Host	Inclusion Type	*N*	Th Range (°C)	Th Mode (°C)	Th Mean (°C)	Salinity Range (wt % NaCl)	Salinity Mode (wt % NaCl)
1R-1 41–44	Diabase	21.93	Qtz-Chl vein	1a	67	147.7–285.0	161.7	180.8	3.1–5.1	3.7
5R-3 107–110	Troctolitic gabbro	39.96	Plg	1b	96	192.0–349.0	277.0	273.0	0.5–1.1	0.5
10R-1 127–129	Gabbro	61.48	Plg	1a/b	82	250.8–320.3	278.9	292.0	0.7–2.9	1.4
40R-1 17–19	Troctolite	214.98	Qtzvein	1a	83	135.0–289.5	210.0	208.7	2.4–3.7	3.4
40R-1 21–24	Tdjh	215.02	Qtz vein	1a	58	124.5–204.9	166.0	161.5	2.9–4.0	3.4
40R-1 21–24	Tdjh	215.02	Qtz	3a	12	314.5–>400.0		388.6	9.5–20.7	17.4
40R-1 21–24	Tdjh	215.02	Qtz	3b	7	336.4–>400.0		383.4	31.1–37.7	

[a]Th = Temperature of homogenization; Qtz = Quartz; Chl = Chlorite; Plg = Plagioclase; Tdjh = Trondjhemite.

Quartz vein-hosted type 1a inclusions (Figures 4a, 4c, and 4d) homogenize in the liquid phase at temperatures of 124.5–289.5°C and show ice melting at −1.4 to −3.1°C, implying salinities of 2.4–5.1 wt % NaCl equivalent (mode = 3.4 ± 1.2 wt % NaCl eq; N = 207) clustering around the seawater value (3.2 wt % NaCl eq; Figures 5 and 6).

Plagioclase-hosted low-salinity type 1b inclusions (Figure 4b) homogenize in the liquid phase at temperatures of 192–349°C and exhibit melting of ice at −0.1 to −1.0°C, indicating salinities of 0.2–2.9 wt % NaCl. Unlike the other samples, the distribution of homogenization temperatures is not unimodal (Figure 6) and the wide range of homogenization temperature is possibly the result of necking down due to fracturing and chlorite filling veins in the vicinity of the inclusions. The mode in salinities is 0.5 wt % NaCl eq (depleted relative to the seawater value); N = 163. In sample U1309D 10R-1 127–129, type 1a inclusions are also present and homogenize in the same range of temperatures at equivalent salinities of 2.0–4.3 wt % NaCl (Figures 5 and 6).

4.2.2. Type 3a: Liquid-Dominated High Salinity [L + V (L)]

Liquid-dominated high-salinity inclusions lacking daughter minerals (type 3a) are found in quartz grains of the trondjhemite sample (U1309D 40R-1 21–24), and are associated with type 3b inclusions. Their primary or secondary origin is not really clear. They are irregular in shape with a range in size of 5–20 μm. Homogenization occurred in the liquid phase at temperatures of 314.5 to >400°C. Melting of ice occurred at −6.2 to −17.6°C, indicating salinities of 9.5–20.7 wt % NaCl (Figure 5); N = 12.

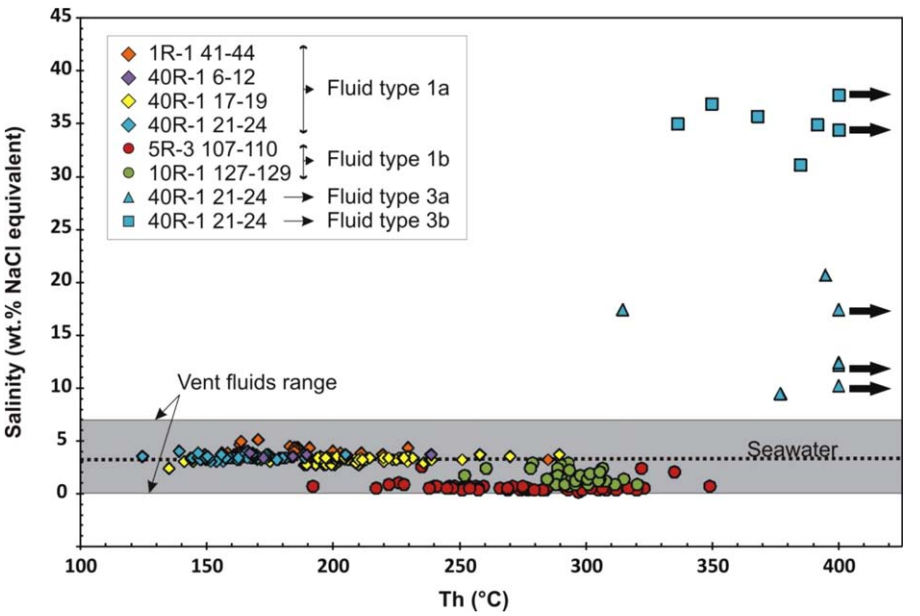

Figure 5. Temperature of homogenization against salinity for all samples. The shaded area represents the range in salinity for fluids exiting submarine hydrothermal vents. Arrows mean that fluid inclusions were not homogenized at this temperature (high temperature limit of apparatus).

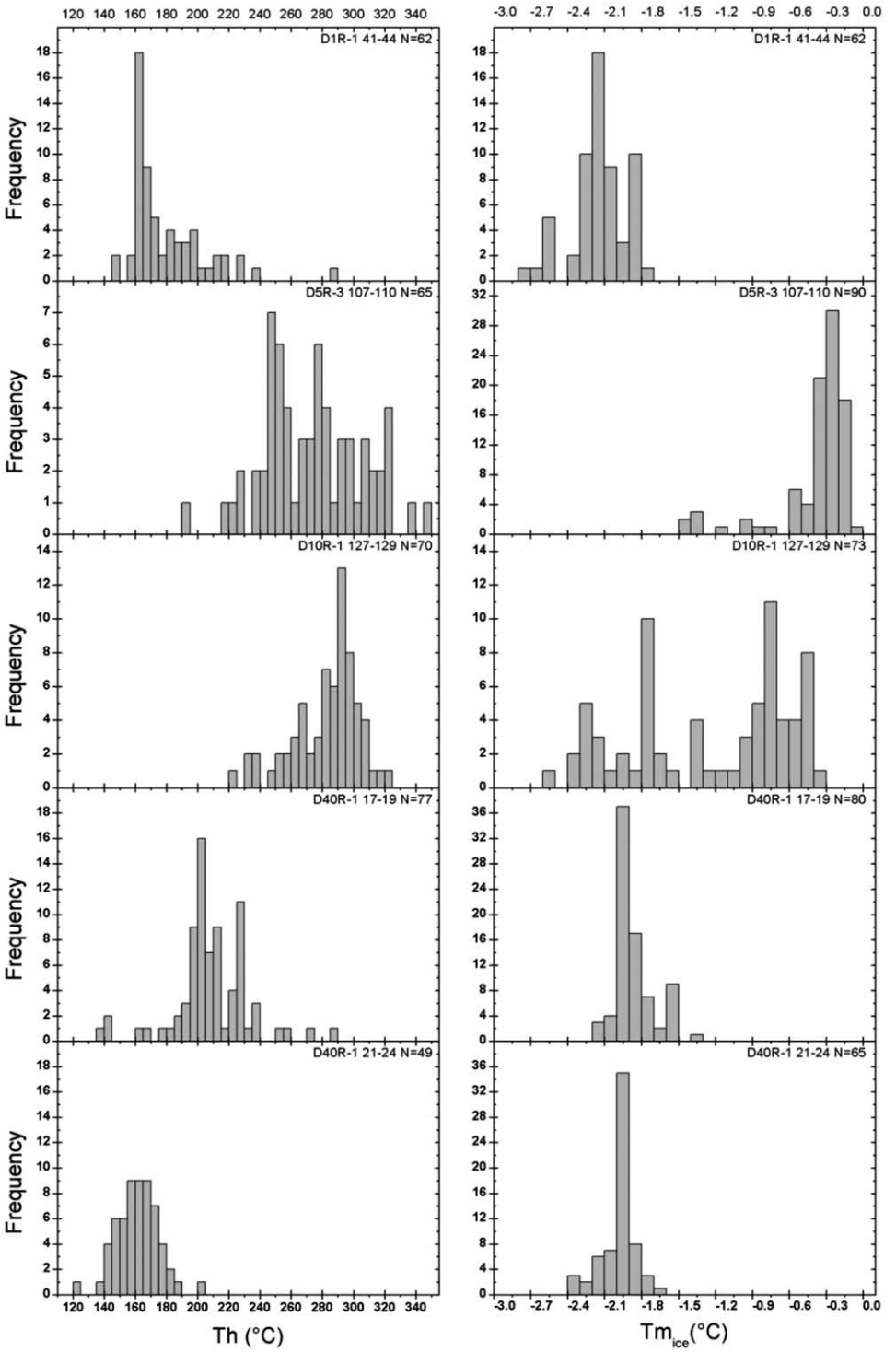

Figure 6. Histograms of homogenization temperatures and of temperatures of melting of ice. For sample U1309D 40R-1 21–24, only results of inclusions in the quartz vein are presented here as insufficient data from inclusions in the quartz grains of the trondjhemite were conducted to obtain good quality statistics.

4.2.3. Type 3b: Daughter Mineral-Bearing Inclusions [L + V + H (L)]

Halite-bearing fluid (type 3b) inclusions have been found in quartz grains of the trondjhemite and are associated with type 3a, although their temporal relationship is not clear. They are irregular in shape with variable size of 10–50 μm, liquid dominated, and rarely contain other daughter minerals (Figure 4e). Dissolution

of the halite cube (184–294°C) always occurred at lower temperatures than the homogenization temperature, marked by the disappearance of the vapor bubble (336.4 to >400°C). Some inclusions remained unhomogenized at a temperature of 400°C (the limit of the stage used). Since halite dissolution had already been observed, the behavior of the vapor bubble suggested that homogenization would occur in the next 20–30°C. The vapor bubble had considerably decreased in volume and was intensely moving around the inclusion. This behavior, observed in all other inclusions, characterizes approach homogenization. These particular inclusions are indicated by arrows on Figure 5. Halite dissolution temperatures indicate equivalent fluid salinities of 31.1–37.7 wt % NaCl eq; N = 7.

Cooling experiments were undertaken in order to test for the presence of additional gas species in the vapor phase, but no clear phase changes were observed.

4.2.4. Liquid-Dominated Related to Chlorite Veins

The elongated cigar shape inclusions that have been observed in plagioclase (Figure 4f) could not be studied microthermometrically because the thickness of the wafer made observation of a single inclusion impossible.

5. Discussion

5.1. Fluid Evolution in Oceanic Core Complexes

The fluids observed in this study could have been trapped at different stages in the evolution of the rocks recovered from the Atlantis Massif. A number of other detachment-related settings in the Atlantic Ocean have been studied [cf. *Escartin and Canales*, 2011], in particular that linked to the TAG hydrothermal field [*deMartin et al*., 2007; *McCaig et al*., 2010]. The Atlantis massif, like many other OCCs, is capped by a talc-tremolite schist formed in the greenschist facies [*Boschi et al*., 2006; *Blackman et al*., 2011], which has been inferred to be the locus for discharge of black smoker fluids [*McCaig et al*., 2007, 2010; *McCaig and Harris*, 2012]. The depth of any melt lens supplying heat to black smoker systems in such a setting is unknown, but may be as deep as 7 kmbsf, [*Canales et al*., 2007; *deMartin et al*., 2007]. The cooling history of the Massif has been constrained by paleomagnetic [*Morris et al*., 2009] and thermochronometric [*Grimes et al*., 2008, 2011; *Schoolmeesters et al*., 2012] data. Our data are interpreted in the framework of the thermal model of *Schoolmeesters et al*. [2012] and the evolution of hydrothermal circulation in the Massif suggested by *McCaig et al*. [2010].

5.2. Hydrostatic and Lithostatic Pressure Gradients

Interpretations of the pressure-temperature conditions of the two-phase curve between liquid and vapor are strongly dependent on the type of fluid pressure which occurs in the crust. Hydrostatic pressure applies to fluids in cracks under brittle conditions. Lithostatic pressure applies to fluids exsolving from a melt under ductile conditions and to fluids isolated from the convective circulation. The switch between those conditions is likely linked to the depth interval of the brittle-ductile transition. Calculations estimate this transition at a temperature of 700–800°C in moderately shallow gabbroic rocks [*Hirth et al*., 1998]. Hydrostatic pressure will be favored in a model where seawater is the fluid source whereas if magmatic fluid is the parent fluid the pressure may be hydrostatic or lithostatic, depending on depth of fluid circulation.

The PT gradient under hydrostatic pressure will vary depending on water temperature. A cold hydrostatic pressure gradient is ~100 bars/km at normal seawater temperature, whereas a hot hydrostatic pressure gradient is ~30 bars/km at black smoker temperature [*Coumou et al*., 2009] (see below and Figure 7). The vertical pressure gradient must be small enough for cold water to flow down in the recharge zone, and large enough for hot water to flow up in the discharge zone, implying the pressure gradient generally lies between cold and hot hydrostatic pressure [*Jupp and Schultz*, 2000]. Nonetheless, several studies [*Jupp and Schultz*, 2004; *Wilcock and McNabb*, 1996] assume that a pressure gradient very close to cold hydrostatic pressure defines the properties of the circulating fluids such as viscosity and flow resistance.

5.3. Pressure and Temperature Conditions of Fluid Entrapment

In OCCs, where the detachment fault is the locus of large fluid flux and the magma chamber is supposed to be approximately at a depth of 7 kmbsf, fluid may circulate from the depth of the seafloor to as deep as 7 kmbsf. We assume a water depth of 3.5 km, as seen at the TAG hydrothermal field. Over this depth range,

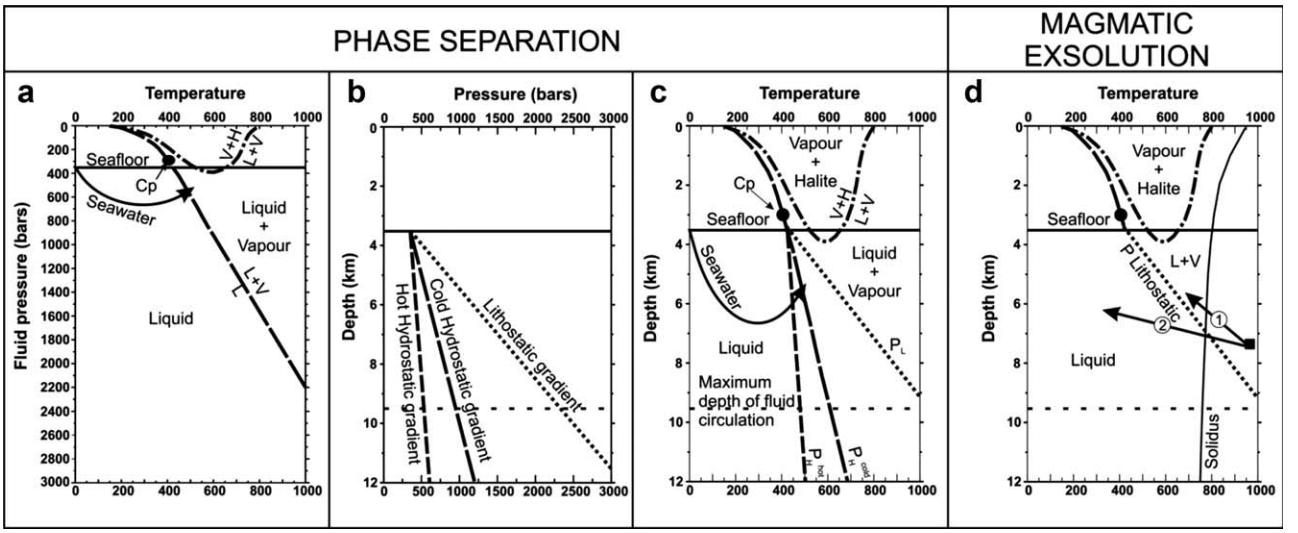

Figure 7. Temperature/fluid pressure and pressure/depth diagrams in the system H_2O-NaCl for a fluid of seawater composition (3.2 wt % NaCl eq). The figure illustrates two processes: (a–c) phase separation and (d) magmatic exsolution. (Figure 7a) Seafloor is at an approximate depth of 3500 m corresponding to the TAG model. The two-phase curve is shown for hydrostatic conditions and separates the single phase liquid field from the two-phase vapor + liquid field [*Sourirajan and Kennedy*, 1962]. The critical point (Cp) of seawater is also shown (407°C, 298 bars) as well as the three phase curve that separates the stability field of liquid and vapor from that of vapor and halite. (b) Relationship between fluid pressure and depth for hydrostatic pressure under cold (100 bars/km) and hot (30 bars/km) gradients [*Coumou et al*., 2009] and a lithostatic pressure gradient. (Figure 7c) The two-phase curve is shown here in a temperature against depth diagram for cold and hot hydrostatic conditions using both diagrams of Figures 7a and 7b, and for lithostatic conditions. In this case, at a given depth, phase separation will occur at higher temperature under lithostatic conditions than under cold hydrostatic conditions, and in turn at higher temperature under cold hydrostatic conditions than under hot hydrostatic conditions. (d) The solidus of a water-saturated tonalite [*Wyllie*, 1977], whose intersection with the two-phase curve under lithostatic pressure separates the crystal + melt + liquid + vapor field from the crystal + melt + liquid field, is plotted. At depth <8 km and temperature > the solidus, an exsolved fluid following path 1 will consist of supercritical droplets of brines in a vapor phase; whereas a fluid exsolving along a path similar to 2 will exsolve as a single phase.

lithostatic pressure would be between approximately 0.35 and 2.45 kbars, respectively, and cold hydrostatic pressure approximately 0.35 and 1.05 kbars, respectively (assuming a rock density of 3000 kg m^{-3}).

A pressure correction is necessary to estimate the temperature of fluid entrapment from the microthermometry. This correction is valid for inclusions that contain pure NaCl solution, for which the salinity of the fluid has been correctly determined, and for which homogenization occurs in the liquid phase, and when pressure of formation can be estimated [*Roedder*, 1984]. The extreme pressures given above correspond to the minimum and maximum hydrostatic and lithostatic pressures that the inclusions experienced on trapping, depending on when they formed during the exhumation of the Atlantis Massif. These pressures allow calculation of isochores (Figure 8) which the fluid inclusions followed from trapping to homogenization while cooling. Pressure-corrected trapping temperatures for fluids with less than 20.8 wt % NaCl were calculated from the software Loner38© from http://fluids.unileoben.ac.at that computes the equations from *Zhang and Frantz* [1987] for the system H_2O-NaCl. Pressure-corrected trapping temperatures for supersaturated fluid were calculated using equation 4 of *Bodnar and Vityk* [1994] that gives dP/dT (bar/°C) as a function of the salinity and the homogenization temperature.

The pressure-temperature conditions described in *Schoolmeesters et al*. [2012] are used here to better constrain the trapping conditions of fluid inclusions. In Figure 8, the intersection of the isochores and the P-T curves of *Schoolmeesters et al*. [2012] gives a range of possible trapping conditions for each individual fluid type. Pressures for the PT curves of *Schoolmeesters et al*. [2012] are calculated assuming either hydrostatic pressure or lithostatic pressure from the depth of the top core pressure/depth-temperature curve in their Figure 6 using a water column of 3500 m and a rock density of 3000 kg m^{-3}. Seawater-like fluid (type 1a) could have been trapped at depths between 1.8 and 3.8 kmbsf and temperatures between 190 and 250°C if in an active buoyancy-driven convective system under hydrostatic conditions. If they were isolated from any active system they could have been trapped deeper and at higher temperatures (2.8 to ~4.2 kmbsf and up to 300°C) (Table 5). Low-salinity fluid with respect to seawater (type 1b) could have been trapped at hydrostatic pressure of 780–800 bars and temperatures up to 290°C. They would have been trapped at greater pressures (up to 1.9 kbars at 460°C) under lithostatic conditions it they were isolated from any active

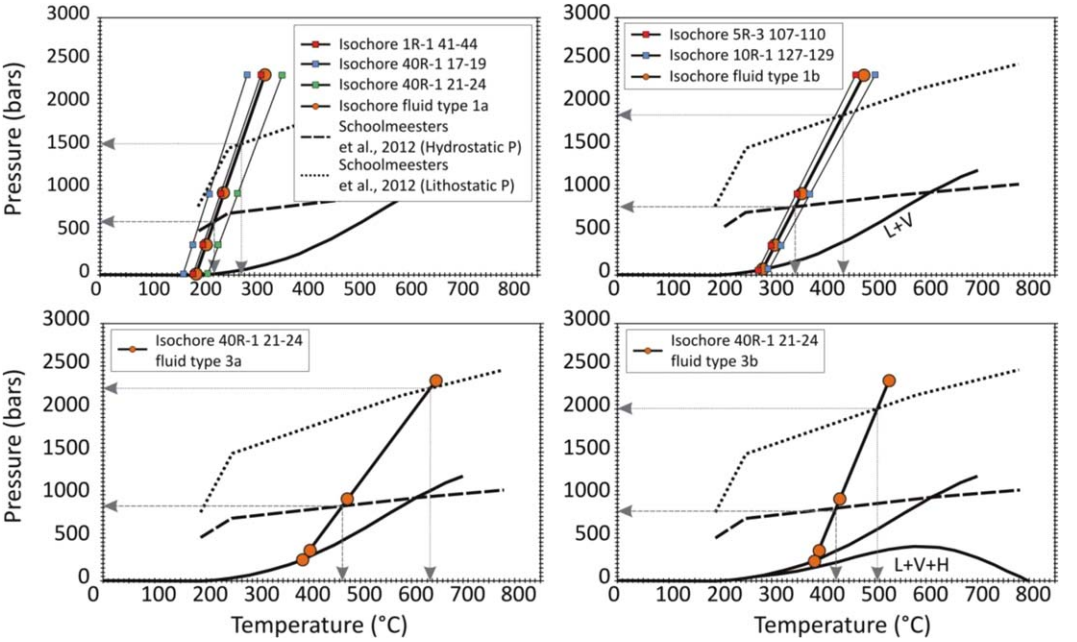

Figure 8. Range of possible trapping conditions for each type of fluid. A range of possible trapping conditions can be read at the intersection between the isochore and the P-T curves from *Schoolmeesters et al*. [2012]. These P-T curves were calculated for hydrostatic and lithostatic gradients from depths in their Figure 6 using a water column of 3500 m (assumed to be the depth at the end of detachment fault movement) and a rock density of 3000 kg m^{-3}. The liquid-vapor curve and the liquid-vapor-halite curve are from *Khaibullin and Borisov* [1966] and *Sourirajan and Kennedy* [1962]. The isochores were calculated with the software Loner38© from http://fluids.unileoben.ac.at and from equation 4 of *Bodnar and Vityk* [1994].

conductive system (Table 5). High-salinity fluid with respect to seawater salinity (type 3a) could have been trapped at hydrostatic pressure of 870 bars and at temperature of 470°C if connected to a convective system whereas it would have been trapped at higher pressure of 2.2 kbars and higher temperature of 635°C if not connected to such system (Table 5). If hypersaline fluids (type 3b) were connected to a conductive system, they could have been trapped at depths of ~5 kmbsf and at temperatures of 430°C. Under lithostatic conditions, these same fluids would have been trapped at greater depths (5.5 kmbsf) and greater temperatures (500°C; Table 5).

5.4. Processes Modifying the Salinity

Several processes have been suggested to explain the variations in salinity observed in fluids circulating in the oceanic crust. They include subcritical phase separation (boiling) or supercritical phase separation (condensation) of a seawater-like fluid [*Kelley et al*., 1993; *Kelley and Malpas*, 1996] or magmatic fluid [*Kelley and*

Table 5. Pressure-Corrected Trapping Temperatures for All Samples and Mean for Each Types of Fluid Inclusion[a]

		P Hydrostatic			P Lithostatic		
	Th Mean (°C)	Tt (°C)	Pt (bars)	Depth t (kmbsf)	Tt (°C)	Pt (bars)	Depth t (kmbsf)
1R-1 41–44	180.8	214	589	2.39	266	1508	3.86
40R-1 17–19	208.7	253	727	3.77	308	1594	4.15
40R-1 21–24	161.5	188	496	1.46	225	1193	2.81
Fluid type 1a mean	185.8	221	616	2.66	273	1523	3.91
5R-3 107–110	273.0	334	783	4.33	422	1828	4.93
10R-1 127–129	292.0	359	799	4.49	461	1907	5.19
Fluid type 1b mean	280.8	344	789	4.39	438	1860	5.03
40R-1 21–24 (3a)	388.6	467	873	5.23	635	2232	6.27
40R-1 21–24 (3b)	383.4	426	845	4.95	505	1997	5.49

[a]Values are calculated with the averages of every type of inclusion, using the P-T curves of *Schoolmeesters et al*. [2012] for both hydrostatic and lithostatic pressure gradients and an assumed water depth of 3.5 km. Th = temperature of homogenization; Tt = temperature of trapping in degree Celsius; Pt = Pressure of trapping in bars; Depth t = Depth of trapping in kmbsf.

Früh-Green, 2001], magmatic fluids exsolving from melts [*Kelley et al*., 1992, 1993; *Kelley and Malpas*, 1996], hydration/dehydration reactions with precipitation/dissolution of associated chloride-bearing minerals [*Kelley and Robinson*, 1990; *Kelley et al*., 1992], and variable mixing of hydrothermal fluid with a phase-separated brine or vapor [*Kelley and Robinson*, 1990]. The most common explanation for the generation of low-salinity fluids is phase separation of seawater-like fluids, and the most usual explanation for generation of high fluid salinities is phase separation of either magmatic or seawater-like fluids. Hydration reactions may also play a role. Variable mixing of hydrothermal seawater with phase-separated brines and vapor can also change the salinity of fluids as a late process.

5.4.1. Hydration/Dehydration

Under rock dominated conditions, hydration reactions or retrograde dissolution of chloride-bearing mineral phases have the potential to modify the ionic strength of hydrothermal fluids by consuming or liberating chloride ions [*Kelley and Robinson*, 1990; *Kelley et al*., 1992]. Formation of secondary amphibole containing up to 4 wt % chlorine [*Vanko*, 1986] can then result in decrease of fluid salinities, and dissolution of such phases might increase fluid salinities [*Seyfried et al*., 1986]. These processes could then account for slight changes in fluid salinity (low-temperature, low-salinity fluid generation) at relatively low water-rock ratio conditions, preferentially in a near axis environment recharge zone [*Kelley et al*., 1995], in contrast to an outflow zone where fluids rapidly pass through the oceanic crust [*Delaney et al*., 1987].

Electron microprobe data (Tables (1–3)) of amphiboles in samples from which microthermometry was undertaken, show Cl/H_2O of 0.000–0.049 with a mean of 0.01 $\pm$ 0.014, whereas Cl/H_2O in seawater is 0.0195. Formation of such amphiboles is unlikely to have influenced salinity of the residual fluid as Cl content is too low compared to that of seawater. The complete collection of electron microprobe data from holes U1309B and U1309D show a Cl/H_2O ratio of 0.000–0.148 with a mean at 0.024 $\pm$ 0.028 (unpublished data of our collection). In general, formation of this type of amphibole cannot account for the great variety of salinity observed in U1309D, but some amphiboles show such high Cl/H_2O (0.148 for the maximum in this study) that precipitation of such minerals can lead to a slight salinity decrease in the residual fluid.

5.4.2. Phase Separation

5.4.2.1 Generation of Brines

Fluid sources and pressure conditions for brine-bearing inclusions are difficult to determine. Brine inclusions homogenize by disappearance of the vapor bubble at temperature $>$400°C. Two models for the generation of brine are as follow:

1. Brine and vapor are generated during supercritical phase separation (condensation) of either magmatic or seawater-derived fluids with segregation of the phases driven by density differences and entrapment of the brine at depth.

2. Direct exsolution of magmatic brine from late stage melts with significant cooling during the migration of the brines along microfractures (Figure 7).

The system H_2O-NaCl will be used in the discussion below as an analog for fluid circulating in the oceanic crust. In a temperature-pressure diagram, the two-phase curve separates the one-phase field (liquid) from the two-phase field (liquid + vapor) at pressure-temperature conditions greater than the critical point of seawater (Cp: 407°C; 298 bars). Fluids of seawater-like salinity or magmatic fluids that circulate at deep levels of the oceanic crust and intersect the two-phase curve will undergo supercritical phase separation (commonly described as condensation) where droplets of brines will separate out of a vapor-rich phase (Figure 7*a*). Fluids circulating under low-pressure conditions will boil and separate a vapor from a low-salinity fluid. However, since a water depth of approximately 3500 mbsf is assumed in our TAG-based model for the Atlantis Massif, boiling cannot happen in this system. In addition, seawater-like fluids in hydrothermal systems mainly circulate at temperatures of 400°C or less [*Coumou et al*., 2009]. According to Figure 7c, fluids which circulate at this temperature and at any depth or pressure will stay in the single phase region, and phase separation is therefore impossible. Fluids need to be heated up by magmatic intrusion such as diabase dikes [*McCaig and Harris*, 2012] to undergo phase separation in this system.

As seawater-like fluids circulate down to depth, fluids will traverse several condensation curves depending on the composition while approaching the heat source [*Kelley et al*., 1993]. For instance, a fluid of seawater composition (3.2 wt % NaCl), which circulates at crustal depth of approximately 2 km and under 550 bars of pressure assuming a water column of 3.5 km and cold hydrostatic conditions, will encounter the two-phase

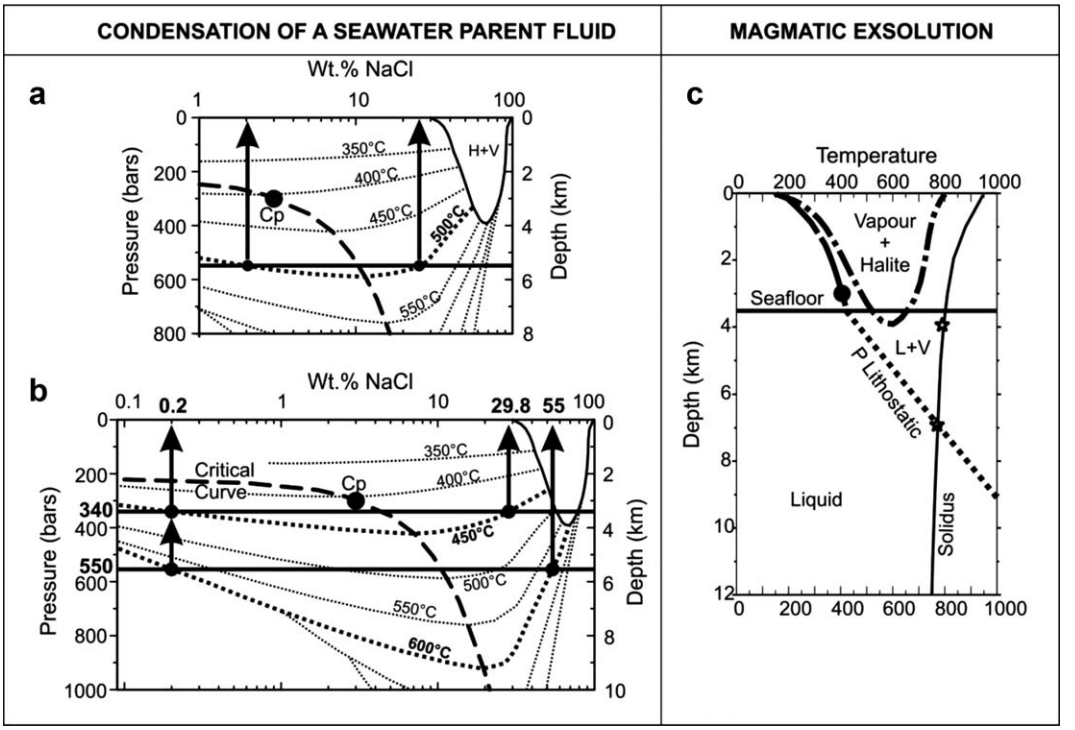

Figure 9. Processes generating variations in salinity observed in the Atlantis Massif. (a) P-X projection of the system H_2O-NaCl contoured for T under hydrostatic conditions. The critical curve (dashed line), the isotherms (dotted lines), and the three phases curve (plain line) are from *Sourirajan and Kennedy* [1962]. A seawater-like fluid which intersects the two-phase curve, at a temperature of 500°C and pressure of ~550 bars will undergo supercritical phase separation (condensation) and separate droplets of brines with salinities of ~25.3 wt % NaCl eq from a vapor of salinity close to 2.2 wt % NaCl equivalent. (b) In this model, it is assumed that the vapor-like fluid generated by phase separation has a salinity of ~0.2 wt % NaCl. That salinity can be obtained under various conditions that will generate different brine salinities. The minimum temperature, at which supercritical phase separation generates a vapor phase of 0.2 wt % NaCl under hydrostatic conditions, is 450°C at a pressure of 340 bars and the maximum temperature is ~600°C at 550 bars. (c) Temperature-depth diagram under hydrostatic conditions above seafloor (dashed line) [*Sourirajan and Kennedy*, 1962] and lithostatic conditions under seafloor (dotted line), showing maximum and minimum conditions for brine generation by exsolution under supercritical conditions and condensation.

curve if heated to 500°C by intrusions, and will condense a fluid containing 25.3 wt % NaCl and a vapor with 2.2 wt % NaCl (Figure 9a). Under hot hydrostatic conditions, the fluid would need to circulate at a total depth of ~10 km—crustal depth of ~6.5 km (Figures 7b and 7c) in order to generate the same result by phase separation at 550 bars and 500°C. This would imply that fluids were trapped almost immediately after being generated since the maximum depth of circulation in the TAG model is 6–7 kmbsf [*Canales et al*., 2007; *deMartin et al*., 2007; *McCaig et al*., 2010]. Higher-salinity fluids (in comparison to seawater) circulating under the same pressure temperature conditions would give the same compositions for brine and vapor, but would separate a bigger proportion of brine. If fluids circulate at shallower levels, they will separate out a greater volume of vapor given the pressure dependence on the shape of the two-phase curve [*Kelley et al*., 1993]. Under lithostatic conditions, the same fluids must be at higher temperature (~600°C) in order to undergo phase separation (Figure 7c).

Generation of hypersaline magmatic brines can be explained by two different processes. Figure 7d shows the two-phase curve for a fluid of seawater salinity (3.2 wt % NaCl eq) for lithostatic conditions and illustrates two scenarios:

1. Exsolution of magmatic fluids under supercritical conditions and condensation of droplets of brines in a vapor phase (Figure 7, path *D1*) [*Kelley and Delaney*, 1987; *Kelley and Früh-Green*, 2001], Fluids in the melt are under lithostatic pressure, and at depth <8 km and at temperature above the solidus, crystal, melt, liquid, and vapor coexist. A fluid exsolving under conditions of the two-phase field will undergo exsolution under supercritical conditions and condensation of immiscible droplets of brine in a vapor phase.

2. Direct exsolution of brines in the absence of a vapor phase (Figure 7, *path D2*). At depths greater than 8 km, the solidus separates a field where solid, melt, and liquid coexist from a field with a single liquid plus

solid, such that any fluid under those conditions would be exsolved as one single phase of uncertain salinity.

Halite-bearing inclusions have been found only in trondjhemite. Trondjhemite being a late magmatic intrusion, a seawater-derived parent fluid is not likely. A magmatic fluid source for generation of hypersaline inclusions seems then to be the most probable. The condensation model is preferably applicable for brines and associated low-salinity vapor-rich inclusions, whereas the direct exsolution of brines model is more applicable to inclusions that homogenize by halite dissolution [*Kelley and Früh-Green*, 2001]. Since hypersaline inclusions in IODP hole U1309D homogenize by vapor disappearance and not by halite dissolution, it is suggested that brines have been formed by exsolution of a magmatic fluid under condensation (Figure 9c). The maximum pressure-temperature conditions are 770°C and ~7 km depth, which is equivalent to ~1.5 kbars according to the lithostatic gradient of Figure 7b. The minimum conditions in terms of pressure depth are 790°C and ~4 km depth, which is equivalent to ~515 bars according to Figure 7b. Note that since it concerns a magmatic intrusion (trondjhemitic intrusion), the maximum conditions seem to be the most probable.

5.4.2.2 Generation of Low-Salinity Fluid

Fluid of low salinity relative to seawater can be generated by phase separation as described above. Trapping of a low-salinity vapor fluid has not been observed. What is in fact observed, are liquid-dominated low-salinity fluids in plagioclase at lower temperature than the brine inclusions. As brine and vapor are segregated after separation by density effects, late mixing between the initial vapor-like fluid with seawater-like fluid can occur to reach the salinity and temperatures of homogenization observed. Note that the phase separation event does not have to be the same event described in the previous paragraph for generation of brine observed in trondjhemite. In the model of Figure 9b, we discuss the conditions for the generation of low-salinity fluid (fluid type 1b) with respect to seawater salinity. It is assumed that the vapor-like fluid generated by phase separation has a salinity of ~0.2 wt % NaCl because that is the minimum salinity of low-salinity inclusions (type 1b) found in the system. That salinity can be obtained at various conditions that will generate different brine salinities. The minimum temperature, at which supercritical phase separation generates a vapor phase of 0.2 wt % NaCl under hydrostatic conditions, is 450°C at a pressure of 340 bars (Figure 9b). However, the minimum hydrostatic pressure possible in the system constrained by our TAG-based AM model is the seafloor pressure (P = 350 bars). The maximum temperature is ~600°C at a hydrostatic pressure of 550 bars (Figure 9b). Such temperatures can most easily be reached if fluids are heated up by dikes or other intrusions [*McCaig and Harris*, 2012] that are formed deep and that are unroofed during exhumation of the massif. However, in both cases, significant cooling must occur in order to reach the trapping temperatures of such inclusions that do not exceed ~345°C on average under hydrostatic conditions and ~440°C on average under the maximum pressure correction at lithostatic conditions. Estimated pressures of trapping based on the *Schoolmeesters et al*. [2012] exhumation curves (790–1860 bars; Figure 8 and Table 5) are much higher than those suggested by our H_2O-NaCl model. At 790 bars under hydrostatic conditions, fluid that intersects the critical curve cannot produce such a low-salinity fluid. It may be that the assumed water depth of 3.5 km in the model is too great, or that some of the assumptions regarding exhumation rate in the *Schoolmeesters et al*. [2012] exhumation paths need adjusting.

5.5. Detachment-Controlled Fluid Discharge—The TAG Model

Tivey et al. [2003] first hypothesized that the TAG hydrothermal field [*Alt and Teagle*, 1998; *Rona et al*., 1993; *Teagle et al*., 1998a, 1998b, 1998c] is located on the hanging wall of an active detachment fault. *deMartin et al*. [2007] studied seismic refraction and microearthquake from the TAG segment and suggested that the TAG hydrothermal field is sited on the hanging wall of a dome-shaped detachment fault that penetrates to depths of >7 km below the seafloor. Their results suggest that high-temperature fluid discharge at TAG is controlled by the detachment fault, a hypothesis supported by evidence that exhumed detachment faults in the Atlantic were the locus of significant fluid flow at black smoker temperatures [*McCaig et al*., 2007, 2010]. A seismic refraction study from *Canales et al*. [2007] also supports this hypothesis and adds that magmatic intrusions at depth (>4 km and perhaps as deep as 7 km) must be the heat source for sustaining the long term, high-temperature hydrothermal circulation at TAG. *McCaig et al*. [2010] interpreted the cross section of *deMartin et al*. [2007] and added isotherms to the model in order to predict the thermal evolution of the TAG detachment fault and its footwall. It is assumed that the configuration of the TAG hydrothermal mound fits the possible early configuration of Atlantis Massif. *Schoolmeesters et al*. [2012] propose a similar

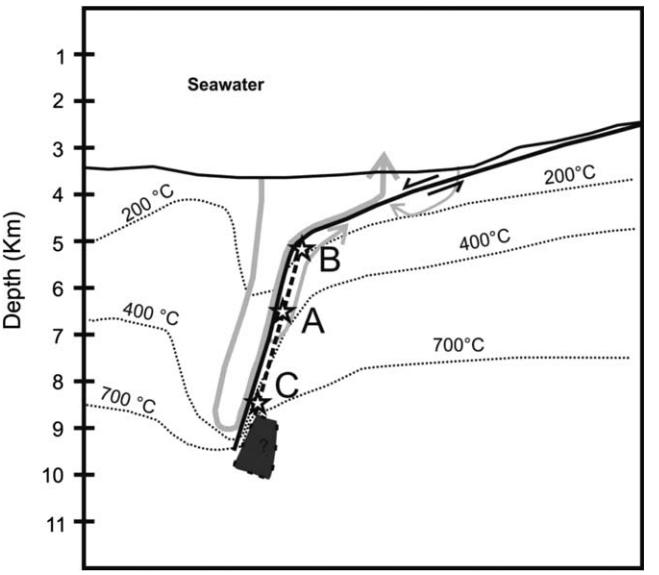

Figure 10. Interpreted cross section for the Atlantis Massif showing the depth of trapping of each type of fluid of IODP Hole U1309D at different times of the fluid history. (a) Late stage quartz precipitation and trapping of type 1a seawater-like salinity fluid. (a and b) Trapping of low-salinity fluid in plagioclase. The vapor fluid phase of a phase-separated, seawater-derived fluid is mixed with recharged seawater. Dashed line shows a schematic dike injection to induce phase separation and generate low-salinity fluid. (c) Trapping of exsolved magmatic fluid generating hypersaline brine observed in trondjhemite. Depth and size of the magma chamber are unknown, but the depth of intrusion is suggested to extend up the footwall of the fault. Isotherms are based on *McCaig et al*. [2010], modified according to the thermochronometric data of *Schoolmeesters et al*. [2012]. Positions of these isotherms away from the detachment fault are speculative.

model with hydrothermal cooling of the detachment fault and its footwall, but with lower fluid temperatures as suggested by thermochronometric data. Thermal balance arguments suggest that large black smoker systems like TAG cannot be continuously active for long periods [*Cannat et al*., 2004], yet TAG has a long history of activity [*Lalou et al*., 1995]. It may be that black smoker circulation was episodic, punctuated by periods of lower temperature flow, with an average temperature consistent with the *Schoolmeesters et al*. [2004] cooling curves. The importance of the TAG model is that fluid is predicted to circulate much deeper than in previous models used to understand fluid inclusion microthermometry in seafloor hydrothermal systems [*Kelley and Delaney*, 1987; *Kelley et al*., 1993, 1995; *Kelley and Malpas*, 1996].

Seawater fluids circulating at 400°C or less should remain in the single phase region throughout (Figure 7c). Figure 8 and Table 5 indicate that these type 1a fluids could have been trapped between 1.5 and 3.8 kmbsf in the *Schoolmeesters et al*. [2012] model at hydrostatic pressures. In Figure 10, this would be between locations A and B. These fluids may have circulated much deeper in the system before being trapped, or they could be recharge fluids. In an active hydrothermal system such fluids would be expected to remain at hydrostatic pressures. However, a trapping pressure of around 900 bars would be required to reconcile the fluid inclusion temperatures with those based on chlorite geothermometry (283–242°C, see section 4) in sample 1R1 41–44. This suggests a trapping pressure between hydrostatic and lithostatic, although the depth of trapping may be little different. These data suggest some cycling of pressure between hydrostatic and higher values, perhaps during quiescent phases of circulation. Small variations in salinity in these fluids may be due to hydration reactions or mixing with type 1b or type 3 fluids.

Type 1b fluids require higher temperatures in their history in order to allow phase separation (Figures 7 and 9). The detachment fault was intruded by diabase dykes, including the host of the vein in U1309D 1R-1 41–44. These contain high-temperature amphiboles [*McCaig and Harris*, 2012], indicating intrusion into a wet zone of hydrothermal flow. In the footwall of the detachment, intrusion of gabbroic magma creating a conductive thermal boundary layer to the hydrothermal system has been suggested [*McCaig and Harris*, 2012]. In either of these circumstances transient temperature increase could lead to phase separation if the pressure is not too high. The low-salinity fluids cooled and mixed with seawater before trapping. Dyke injection could have happened between locations A and B.

Finally, we suggest that the hypersaline type 3 inclusions formed by magmatic exsolution of fluid, which could occur either in the single- or two-phase region depending on pressure. If the melt lens was at a depth of 7 kmbsf as suggested by *de Martin et al*. [2007], this would be too deep to allow exsolution in the two-phase region according to Figure 9c, but this diagram assumes seawater salinity and it is not clear what the salinity of a single phase fluid exsolving from a melt would be. Melt could also have intruded shallower as suggested by the range of U-Pb zircon ages reported by *Grimes et al*. [2008]. These fluids were not trapped

at magmatic temperatures, but at temperatures of 505–635°C assuming lithostatic conditions (Table 5). The fact that the inclusions occur as secondary inclusion within quartz grains in a trondjhemite suggests that the brine may have been carried upward within the host intrusion before being remobilized into the observed fluid inclusions. This may have occurred as result of hydrofracture as the lithostatic pressure fluid was decompressed by exhumation. Based on Figure 8, we have suggested a depth of around 5 kmbsf for the trapping of these inclusions, with exsolution from the melt occurring somewhat deeper. The trondjhemite (sample 40R1 21–24) was then cut by a crack-seal quartz vein containing type 1a fluid inclusions. This likely happened at higher levels, between A and B, and in a hydrostatic regime, although lithostatic fluids cannot be ruled out.

The pattern of circulation shown in Figure 10 is highly schematic, and in reality both up and downflow zones are likely to be focused within the fault zone in the third dimension. It is also likely that fluid flow was episodic, with strong upflow events at black smoker temperatures of 350–400°C triggered by magmatic intrusion and intervening periods of less intense, lower temperature circulation [*McCaig et al*., 2010].

6. Conclusions

Fluid inclusion microthermometry demonstrates the occurrence of four different types of fluids in IODP Hole U1309D with different salinities (ranging from 1.4 to 35 wt % NaCl eq) and homogenization temperatures (160 to >400°C). The lowest homogenization temperature is exhibited by fluid trapped in quartz veins (type 1a), and the highest by fluid type 3.

High-salinity (Type 3b) fluid, only found in the evolved trondjhemite intrusion, is proposed to have been generated by condensation of a magmatic fluid at maximum temperature of 770°C at depth of 5–6 kmbsf. These fluids were trapped as fluid inclusions at somewhat lower temperatures during exhumation of the trondjhemite.

Low-salinity fluids (Type 1b), only found in plagioclase, are believed to have been generated by mixing between seawater-derived fluid and supercritical phase-separated seawater at temperatures of 450–600°C and pressures of 340–550 bars and are assumed to have been trapped at a depth of ~3 kmbsf. Black smoker fluids do not normally circulate at such temperatures and it is suggested that phase separation occurred due to injection of dikes.

A late stage fracturing event has provoked precipitation of quartz veins at low pressure (450 bars) and temperature (210°C) that have trapped seawater-like salinity fluid after the footwall had been excavated to shallower depths. Comparison with chlorite geothermometry results suggests that these inclusions may have been trapped at suprahydrostatic pressures, possibly during relatively quiescent phases of fluid circulation.

Results show that the TAG model of *McCaig et al*. [2010], with temperature data refined by *Schoolmeesters et al*. [2012] provides a good framework for explaining the fluid evolution at the Atlantis Massif.

Acknowledgments
The authors thank Damon Teagle and Bruce Yardley for constructive reviews of the PhD thesis from which this work is taken. They also thank Joe Cann for all the interesting general discussions on mid-Ocean Ridges and hydrothermal alteration processes. They finally thank Nick Hayman, the anonymous reviewer, and associate editor Gretchen Früh-Green for the constructive remarks that lead to the reorganization and improvement of the manuscript. Teddy Castelain was funded by grant NE/D001366/1.

References

Alt, J. C., and D. A. H. Teagle (1998), Probing the TAG hydrothermal mound and stockwork: Oxygen-isotopic profiles from deep ocean drilling, in *Proceedings of the Ocean Drilling Program, Scientific Results*, vol. 158, edited by P. M. Herzig et al., pp. 285–295, Ocean Drill. Program, College Station, Tex.

Blackman, D. K., and J. A. Collins (2010), Lower crustal variability and the crust/mantle transition at the Atlantis Massif oceanic core complex, *Geophys. Res. Lett.*, *37*, L24303, doi:10.1029/2010GL045165.

Blackman, D. K., et al. (2002), Geology of the Atlantis Massif (Mid-Atlantic Ridge, 30°N): Implications for the evolution of an ultramafic oceanic core complex, *Mar. Geophys. Res.*, *23*, 443–469.

Blackman, D. K., B. Ildefonse, B. E. John, Y. Ohara, D. J. Miller, C. J. McLeod, and E. Scientists (2006), Expedition 304/305 summary, in *Proceedings of the Integrated Ocean Drilling Program*, vol. 304/305, pp. 1–60, College Station, Tex.

Blackman, D. K., et al. (2011), Drilling constraints on lithospheric accretion and evolution at Atlantis Massif, mid-Atlantic Ridge 30°N, *J. Geophys. Res.*, *116*, B07103, doi:10.1029/2010JB007931.

Bodnar, R. J. (1993), Revised equation and table for determining the freezing point depression of H_2O-NaCl solutions, *Geochim. Cosmochim. Acta*, *57*, 683–684.

Bodnar, R. J., and M. O. Vityk (1994), Interpretation of microthermometric data for H_2O–NaCl fluid inclusions, in *Fluid Inclusions in Minerals, Methods and Applications*, edited by B. De Vivo and M. L. Frezzotti, pp. 117–130, Virginia Tech, Blacksburg, Va.

Boschi, C., G. L. Früh-Green, A. Delacour, J. A. Karson, and D. S. Kelley (2006), Mass transfer and fluid flow during detachment faulting and development of an oceanic core complex, Atlantis Massif (MAR 30°N), *Geochem. Geophys. Geosyst.*, *7*, Q01004, doi:10.1029/2005GC001074.

Canales, J. P., R. A. Sohn, and B. J. deMartin (2007), Crustal structure of the Trans-Atlantic Geotraverse (TAG) segment (Mid-Atlantic Ridge, 26°10′N): Implications for the nature of hydrothermal circulation and the detachment faulting at slow spreading ridges, *Geochem. Geophys. Geosyst.*, *8*, Q08004, doi:10.1029/2007GC001629.

Canales, J. P., B. E. Tucholke, M. Xu, J. A. Collins, and D. DuBois (2008), Seismic evidence for large-scale compositional heterogeneity of oceanic core complexes, *Geochem. Geophys. Geosyst.*, *9*, Q08002, doi:10.1029/2008GC002009.

Cann, J. R., D. K. Blackman, D. K. Smith, E. McAllister, B. Janssen, S. Mello, E. Avgerinos, A. R. Pascoe, and J. Escartin (1997), Corrugated slip surfaces formed at ridge-transform intersections on the Mid-Atlantic Ridge, *Lett. Nat.*, *385*, 329–332.

Cannat, M. (1993), Emplacement of mantle rocks in the seafloor at midocean ridges, *J. Geophys. Res.*, *98*, 4163–4172, doi:10.1029/92JB02221.

Cannat, M., J. R. Cann, and J. Maclennan (2004), Some hard rock constraints on the supply of heat to mid-ocean ridges, in *Mid-Ocean Ridges: Hydrothermal Interactions Between the Lithosphere and Oceans, Geophys. Monogr. Ser.*, vol. 148, edited by C. German, J. Lin, and L. M. Parson, pp. 111–149, AGU, Washington, D. C.

Cathelineau, M., and D. Nieva (1985), A chlorite solid solution geothermometer. The Los Azufres (Mexico) geothermal system, *Contrib. Mineral. Petrol*, *91*, 235–244.

Coumou, D., T. Driesner, S. Geiger, A. Paluszny, and C. A. Heinrich (2009), High-resolution three-dimensional simulations of mid-ocean ridge hydrothermal systems, *J. Geophys. Res.*, *114*, B07104, doi:10.1029/2008JB006121.

Delaney, J. R., D. W. Mogk, and M. J. Mottl (1987), Quartz-cemented breccias from the Mid-Atlantic Ridge: Samples of a high-salinity hydrothermal upflow zone, *J. Geophys. Res.*, *92*, 9175–9192.

deMartin, B. J., R. A. Sohn, J. P. Canales, and S. E. Humphris (2007), Kinematics and geometry of active detachment faulting beneath the TAG hydrothermal field on the Mid-Atlantic Ridge, *Geology*, *35*, 711–714.

Escartín, J., and J. P. Canales (2011), Detachments in Oceanic lithosphere: Deformation, magmatism, fluid flow and ecosystems, *EOS Trans. AGU*, *92*, 31, doi:10.1029/2011EO040003.

Frost, B. R., J. S. Beard, A. M. McCaig, and E. Condliffe (2008), The formation of micro-rodingite from IODP Hole U1309D: Key to understanding the process of serpentinization, *J. Petrol.*, *49*(9), 1579–1588.

Grimes, C. B., B. E. John, M. J. Cheadle, and J. L. Wooden (2008), Protracted construction of gabbroic crust at a slow spreading ridge: Constraints from $^{206}Pb/^{238}U$ zircon ages from Atlantis Massif and IODP Hole U1309D (30°N, MAR), *Geochem. Geophys. Geosyst.*, *9*, Q08012, doi:10.1029/2008GC002063.

Grimes, C. B., M. J. Cheadle, B. E. John, P. W. Reiners, and J. L. Wooden (2011), Cooling rates and the depth of detachment faulting at oceanic core complexes: Evidence ffrom zircon Pb/U and U-Th/He ages, *Geochem. Geophys. Geosyst.*, *12*, Q0AG01, doi:10.1029/2010GC003391.

Henig, A. S., D. K. Blackman, A. J. Harding, J.-P. Canales, and G. M. Kent (2012), Downward continued multi-channel seismic refraction analysis of Atlantis Massif oceanic core complex, 30°N Mid-Atlantic Ridge, *Geochem. Geophys. Geosyst.*, *13*, Q0AG07, doi:10.1029/2012GC004059.

Hirth, G., J. Escartin, and J. Lin (1998), The rheology of the lower oceanic crust: Implications for lithospheric deformation at mid-ocean ridges, in *Faulting and Magmatism at Mid-Ocean Ridges*, edited by W. R. Buck et al., pp. 291–303, AGU, Washington, D. C.

Ildefonse, B., D. Blackman, B. E. John, Y. Ohara, D. J. Miller, C. J. MacLeod, and IODP Expeditions 304/305 Science Party (2007), Oceanic core complexes and crustal accretion at slow spreading ridges, *Geology*, *35*, 623–626.

Jupp, T., and A. Schultz (2000), A thermodynamic explanation for black-smoker temperatures, *Nature*, *403*(6772), 880–883.

Jupp, T. E., and A. Schultz (2004), Physical balances in subseafloor hydrothermal convection cells, *J. Geophys. Res.*, *109*, B05101, doi:10.1029/2003JB002697.

Kelley, D. S. (1996), Methane-rich fluids in the oceanic crust, *J.Geophys. Res.*, *101*, 2943–2962, doi:10.1029/95JB02252.

Kelley, D. S. (1997), Fluid evolution in slow spreading environments, in *Proceedings of the Ocean Drilling Program, Scientific Results*, vol. 153, edited by J. A. Karson et al., pp. 399–415, Ocean Drill. Program, College Station, Tex.

Kelley, D. S., and J. R. Delaney (1987), Two-phase separation and fracturing in mid-ocean ridge gabbros at temperatures greater than 700C, *Earth Planet. Sci. Lett.*, *83*, 53–66.

Kelley, D. S., and G. L. Früh-Green (2001), Volatile lines of descent in submarine plutonic environments: Insights from stable isotope and fluid inclusion analyses, *Geochim. Cosmochim. Acta*, *65*(19), 3325–3346.

Kelley, D. S., and J. Malpas (1996), Melt-fluid evolution in gabbroic rocks from Hess Deep, in *Proceedings of the Integrated Ocean Drilling Program, Scientific Results*, edited by C. Mével et al., pp. 213–226, Ocean Drill. Program, College Station, Tex.

Kelley, D. S., and P. T. Robinson (1990), Development of brine-dominated hydrothermal system at temperature of 400–500°C in the upper level plutonic sequence, Troodos ophiolite, Cyprus, *Geochim. Cosmochim. Acta*, *54*, 653–661.

Kelley, D. S., P. T. Robinson, and J. G. Malpas (1992), Processes of brine generation and circulation in the oceanic crust: Fluid inclusion evidence fron the Troodos ophiolite, Cyprus, *J. Geophys. Res.*, *97*, 9307–9322.

Kelley, D. S., K. M. Gillis, and G. Thompson (1993), Fluid evolution in submarine magma-hydrothermal systems at the Mid-Atlantic Ridge, *J. Geophys. Res.*, *98*, 19,579–19,596.

Kelley, D. S., D. A. Vanko, and C. Gu (1995), Fluid evolution in oceanic crustal layer 2: Fluid inclusion evidence from the sheeteed dike complex, Hole 504B, Costa Rica Rift, in *Proceedings of the Ocean Drilling Program, Scientific Results*, vol. 137/140, edited by J. Erzinger et al., pp. 191–198, Ocean Drill. Program, College Station, Tex.

Khaibullin, I. Kh., and N. M. Borisov (1966), Experimental investigation of the thermal properties of aqueous and vapor solutions of sodium and potassium chlorides at phase equilibrium, *High Temp.*, *4*, 489–496.

Lalou, C., J.-L. Reyss, E. Brichet, P. A. Rona, and G. Thompson (1995), Hydrothermal activity on a 105-year scale at a slow spreading ridge, TAG hydrothermal field, Mid-Atlantic Ridge 26°N, *J.Geophys. Res.*, *100*, 17,855–17,862, doi:10.1029/95JB01858.

McCaig, A. M., and M. Harris (2012), Hydrothermal circulation and the dike-gabbro transition in the detachment mode of slow seafloor spreading, *Geology*, *40*, 367–370, doi:10.1130/G32789.1.

McCaig, A. M., R. A. Cliff, J. Escartin, A. E. Fallick, and C. J. MacLeod (2007), Oceanic detachment faults focus very large volumes of black smoker fluids, *Geology*, *35*, 935–938, doi:10.1130/G23657A.1.

McCaig, A. M., A. Delacour, A. E. Fallick, T. Castelain, and G. L. Früh-Green (2010), Detachment fault control on hydrothermal circulation systems: Interpreting the subsurface beneath the TAG hydrothermal field using the isotopic and geological evolution of Oceanic Core Complexes in the Atlantic, in *Diversity of Hydrothermal Systems on, Slow Spreading Ridges, Geophys. Monogr. Ser.*, vol. 108, edited by P. A. Rona et al., pp. 207–240, AGU, Washington, D. C.

Morris, A., J. S. Gee, N. Pressling, B. E. John, C. J. MacLeod, C. B. Grimes, and R. C. Searle (2009), Footwall rotation in an oceanic core complex quantified using reoriented Integrated Ocean Drilling Program core samples, *Earth Planet. Sci. Lett.*, *287*, 217–228.

Roedder, E. (1984), Fluid inclusions, Mineralogical Society of America, *Reviews in Mineralogy*, *12*, i-vi + 646.
Rona, P. A., M. D. Hannington, C. V. Raman, G. Thompson, M. K. Tivey, S. E. Humphris, C. Lalou, and S. Peterson (1993), Active and relict seafloor hydrothermal mineralization at the TAG hydrothermal field, Mid-Atlantic Ridge, *Econ. Geol.*, *88*, 1987–2013.
Schoolmeesters, N., M. J. Cheadle, B. E. John, P. W. Reiners, J. Gee, and C. B. Grimes (2012), The cooling history and the depth of the detachment faulting at the Atlantis Massif oceanic core complex, *Geochem. Geophys. Geosyst.*, *13*, Q0AG12, doi:10.129/2012GC004314.
Seyfried, W. E., M. E. Berndt, and D. R. Janecky (1986), Chloride depletions and enrichments in seafloor hydrothermal fluids: Constraints from experimental basalt alteration studies, *Geochim. Cosmochim. Acta*, *50*, 459–475.
Sourirajan, S., and G. C. Kennedy (1962), The system H_2O-NaCl at elevated temperatures and pressures, *Am. J. Sci.*, *260*(2), 115–141.
Sterner, S. M., D. L. Hall, and R. J. Bodnar (1988), Synthetic fluid inclusions. V. Solubility relations in the system NaCl-KCl-H_2O under vapor-saturated conditions, *Geochim. Cosmochim. Acta*, *52*, 989–1005.
Teagle, D. A. H., J. C. Alt, H. Chiba, and A. N. Halliday (1998a), Dissecting an active hydrothermal deposit: The strontium and oxygen isotopic anatomy of the TAG hydrothermal mound_anhydrite, in *Proceedings of the Ocean Drilling Program, Scientific Results*, vol. 158, edited by P. M. Herzig et al., pp. 129–141, Ocean Drill. Program, College Station, Tex.
Teagle, D. A. H., J. C. Alt, S. E. Humphris, and A. N. Halliday (1998b), Dissecting an active hydrothermal deposit: The strontium and oxygen isotopic anatomy of the TAG hydrothermal mound-whole rock and silicate minerals, in *Proceedings of the Ocean Drilling Program, Scientific Results*, vol. 158, edited by P. M. Herzig, et al., pp. 297–309, Ocean Drill. Program, College Station, Tex.
Teagle, D. A. H., J. C. Alt, S. E. Humphris, and A. N. Halliday (1998c), Strontium and oxygen isotopic constraints on fluid mixing, alteration and mineralization in the TAG hydrothermal deposit, *Chem. Geol.*, *149*, 1–24.
Tivey, M. A., H. Schouten, and M. C. Kleinrock (2003), A near-bottom magnetic survey of the Mid-Atlantic Ridge axis at 26°N: Implications for the tectonic evolution of the TAG segment, *J. Geophys. Res.*, *108*(B5), 2277, doi:10.1029/2002JB001967.
Tucholke, B. E., J. Lin, and M. C. Kleinrock (1998), Megamullions and mullions structure defining oceanic metamorphic core complexes on the Mid-Atlantic Ridge, *J. Geophys. Res.*, *103*, 9857–9866, doi:10.1029/98JB00167.
Vanko, D. A. (1986), High chlorine amphiboles from oceanic rocks: Product of highly-saline hydrothermal fluids, *Am. Mineral.*, *71*, 51–59.
Vanko, D. A., and D. S. Stakes (1991), Fluids in oceanic layer 3: Evidence from veined rocks, Hole 735B, Southwest Indian Ridge, in *Proceeding of the Ocean Drilling Program Scientific Results*, vol. 118, edited by R. P. Von Herzen et al., pp. 181–215, College Station, Tex.
Wilcock, W. S. D., and A. McNabb (1996), Estimates of crustal permeability on the endeavour segment of the Juan de Fuca mid-ocean ridge, *Earth Planet. Sci. Lett.*, *138*, 83–91.
Wyllie, P. J. (1977), Crustal anatexis—Experimental review, *Tectonophysics*, *43*(1–2), 41–71.
Zhang, Y.-G., and J. D. Frantz (1987), Determination of the homogenization temperature and densities of supercritical fluids in the system NaCl-KCl-$CaCl_2$-H_2O using synthetic fluid inclusions, *Chem. Geol.*, *64*, 335–350.